J. Fluid Mech. (2005), *vol.* 525, *pp.* 73–104.
DOI: 10.1017/S0022112004002563 Printed in the United Kingdom

Sedimentation of hard-sphere suspensions at low Reynolds number

By NHAN-QUYEN NGUYEN AND ANTHONY J. C. LADD

Department of Chemical Engineering, University of Florida, Gainesville, Florida 32611-6005, USA
ladd@che.ufl.edu

(Received 6 July 2004 and in revised form 21 September 2004)

Lattice-Boltzmann simulations have been used to investigate low-Reynolds-number settling of monodisperse and polydisperse suspensions. We confirm the discovery that particle velocity fluctuations are strongly suppressed by no-slip walls at the top and bottom of the system, even in regions distant from the boundaries. We also show that a monodisperse suspension develops a strongly anisotropic long-range microstructure during the settling process, with vanishing density fluctuations in the horizontal plane. We find no numerical evidence that the particle concentration in the bulk is stratified; diffusive spreading of the suspension–supernatant interface is suppressed by hindered settling, as would be expected in moderately concentrated suspensions.

Long-range correlations in particle density fluctuations are destroyed by polydispersity in particle size, and in this case density fluctuations are finite at all length scales and in all directions. However, in polydisperse suspensions there is significant stratification, due to differential settling rather than interface diffusion, which provides an alternative mechanism for screening the hydrodynamic interactions. It is possible that this is the dominant mechanism for hydrodynamic screening in several laboratory experiments.

1. Introduction

Particles larger than a few microns tend to settle out of suspension, because gravitational forces dominate over the diffusive flux arising from gradients in particle concentration. When a suspension settles, each particle experiences a different shielding of the fluid drag, owing to the fluctuating arrangements of its neighbours (Ham & Homsy 1988). These hydrodynamic interactions are long range, decaying asymptotically as the inverse interparticle separation, and drive large fluctuations in particle velocity. For particles more than about 10 μm in diameter, hydrodynamic diffusion completely dominates the thermal Brownian motion. The detailed dynamics of the most idealized flow, the sedimentation of hard spheres in the absence of inertia and Brownian motion is still controversial. A straightforward calculation shows that, if the particle positions are independently and uniformly distributed, the velocity fluctuations are proportional to the linear dimension of the container (Caflisch & Luke 1985). However, two different sets of experiments found that the velocity fluctuations converge to a fixed value for sufficiently large systems (Nicolai & Guazzelli 1995; Segré, Herbolzheimer & Chaikin 1997). The qualitative discrepancy between theory and experiment has generated considerable attention, focusing on possible mechanisms for screening the hydrodynamic interactions and thereby saturating the velocity fluctuations when the system size is larger than the screening length.

The key theoretical idea (Koch & Shaqfeh 1991) is that hydrodynamic interactions can be screened by changes in suspension microstructure, analogous to the screening of electrostatic interactions in charged systems. Hydrodynamic screening occurs when a test particle and its neighbours are collectively neutrally buoyant with respect to the bulk suspension; in other words, when density fluctuations at length scales larger than the screening length are suppressed. This requires a rather delicate long-range correlation in the distribution of particle pairs that is resistant to the randomizing effects of hydrodynamic dispersion. Several different bulk mechanisms for the microstructural changes have been proposed, including three-body hydrodynamic interactions (Koch & Shaqfeh 1991), a convective instability (Tong & Ackerson 1998), and a coupled convection–diffusion model (Levine *et al.* 1998; Ramaswamy 2001). However, these theories are all inconsistent with the results of numerical simulations (Ladd 1993, 1996, 1997), which have shown that in homogeneous suspensions (with periodic boundary conditions) particles are distributed randomly at separations beyond a few particle diameters, and the velocity fluctuations therefore remain proportional to container size.

More recently, the role of the container boundaries has been explored in detail (Brenner 1999; Ladd 2002; Tee *et al.* 2002; Mucha & Brenner 2003; Mucha *et al.* 2004; Nguyen & Ladd 2004). The primary goal has been to discover if container walls can qualitatively change the hydrodynamic interactions in the bulk suspension. Brenner (1999) analysed the effects of vertical container walls on the particle velocity fluctuations, but found that they do not eliminate the system size dependence. However, numerical simulations (Ladd 2002) subsequently showed that rigid boundaries at the top and bottom of the vessel cause a strong time-dependent damping of the velocity fluctuations even in bulk regions far from the walls. These boundaries introduce interfaces between sediment, suspension and supernatant fluid, which are absent in systems with periodic boundary conditions. The time-dependent damping of the velocity fluctuations was explained by convective draining of large-scale fluctuations in particle density to these interfaces (Ladd 2002), a suggestion made earlier by Hinch (1988). A different picture of the effect of container walls was proposed independently, and more or less simultaneously (Tee *et al.* 2002), where it was suggested that hydrodynamic dispersion at the suspension–supernatant interface leads to a stratification in the particle concentration. A stratified suspension introduces another length scale, beyond which the hydrodynamic interactions are screened (Luke 2000). However, a model based on convection of density fluctuations (Nguyen & Ladd 2004) leads to qualitatively different conclusions from a stratified suspension (Mucha & Brenner 2003; Mucha *et al.* 2004); we will compare these ideas with the results of our simulations in §§4.1 and 5.1.

Recent experimental results have cast doubt on the conclusion that the velocity fluctuations necessarily reach a steady state that is independent of system size. Bernard-Michel *et al.* (2002) did not observe a convincing saturation of the velocity fluctuations over comparable cell sizes to Segré *et al.* (1997). Tee *et al.* (2002) found that for large cells the fluctuations decayed for the duration of the experiment, no matter what the height of the container; these observations were explained by an increasing stratification of the suspension with time. Other experiments found that the velocity fluctuations were eventually stationary and independent of system size, even in very large vessels (Guazzelli 2001). To make further progress, it will be necessary to reconcile the apparently conflicting experimental results, and to develop the correct physical picture underlying the screening of the hydrodynamic interactions in settling suspensions. At that point, it may be possible to construct a statistical–mechanical theory along lines proposed earlier (Ramaswamy 2001).

The focus of the present work is on the microstructure of a settling suspension, as characterized by the distribution of pairs of particles in the bulk suspension. At low Reynolds numbers, the instantaneous particle velocities are completely determined by the particle positions, and it can be shown that the dominant contribution to the velocity fluctuations can be calculated from the structure factor (Ladd 1993; Levine *et al.* 1998),

$$S(\boldsymbol{k}) = N^{-1} \sum_{i,j=1}^{N} \exp(-\mathrm{i}\boldsymbol{k} \cdot \boldsymbol{r}_{ij}), \tag{1.1}$$

which is the Fourier transform of the pair correlation function. The effects of hydrodynamic screening show up in the long-wavelength (small k) behaviour of S; an asymptotic k^2-dependence of the structure factor indicates screening and an eventual saturation of the velocity fluctuations with increasing container size. It has not proved possible to measure $S(\boldsymbol{k})$ directly by light scattering, owing to the large size of the particles, but direct imaging has been used to measure related spatial fluctuations in particle concentration (Lei, Ackerson & Tong 2001). In our simulations we have been able to determine the structure factor directly, which is the quantity of greatest theoretical interest. A preliminary account of this work has already been published (Nguyen & Ladd 2004). Here, we present a detailed account of our results for both the velocity fluctuations and the microstructure, including effects of polydispersity, which may be crucial in interpreting experimental results.

2. Simulation method

The computational problem of simulating the coupled dynamics of solid particles within a continuum fluid has been approached in several different ways, with either time-independent or time-dependent (inertial) fluid dynamics. In the time-independent approach, which encompasses Stokesian dynamics (Brady & Bossis 1988; Durlofsky, Brady & Bossis 1987) and boundary-element methods (Pozrikidis 1993; Muldowney & Higdon 1995; Loewenberg & Hinch 1996), the fluid flow field is calculated in the quasi-stationary Stokes-flow approximation, whereas in time-dependent methods the dynamics of fluid and particles evolve simultaneously on the inertial time scale. Time-dependent methods include grid-based schemes, such as finite-difference (Feng, Hu & Joseph 1994*a*, *b*) and lattice-Boltzmann methods (Ladd & Verberg 2001), and particle-based models, such as dissipative-particle-dynamics (Hoogerbrugge & Koelman 1992) and smooth-particle-hydrodynamics (Zhu, Fox & Morris 1999). A comparison of some of the available methods is contained in the review by Ladd & Verberg (2001). In this work, we use the lattice-Boltzmann model for the fluid phase and a coupling between the solid particles and fluid that was first described in Ladd (1994*a*, *b*). The most up-to-date description of the algorithm is given in Ladd & Verberg (2001) and Nguyen & Ladd (2002); here we summarize the key ideas.

2.1. *Lattice-Boltzmann equation*

The fundamental quantity in the lattice-Boltzmann model is the discretized one-particle velocity distribution function $n_i(\boldsymbol{r}, t)$, which describes the mass density of particles with velocity $\boldsymbol{c}_i$, at a particular node of the lattice $\boldsymbol{r}$, at a discrete time t. The hydrodynamic fields, mass density ρ, momentum density $\boldsymbol{j} = \rho\boldsymbol{u}$, and momentum flux $\boldsymbol{\Pi}$, are moments of this velocity distribution:

$$\rho = \sum_i n_i, \quad \boldsymbol{j} = \sum_i n_i \boldsymbol{c}_i, \quad \boldsymbol{\Pi} = \sum_i n_i \boldsymbol{c}_i \boldsymbol{c}_i. \tag{2.1}$$

The time evolution of $n_i(\boldsymbol{r}, t)$ is described by a discrete analogue of the Boltzmann equation (Frisch *et al.* 1987),

$$n_i(\boldsymbol{r} + \boldsymbol{c}_i \Delta t, t + \Delta t) = n_i(\boldsymbol{r}, t) + \Delta_i [\boldsymbol{n}(\boldsymbol{r}, t)], \tag{2.2}$$

where Δ_i is the change in n_i owing to instantaneous collisions at the lattice nodes and Δt is the time step. The collision operator Δ_i is usually constructed by linearizing about the local equilibrium $\boldsymbol{n}^{eq}$ (Higuera, Succi & Benzi 1989), i.e.

$$\Delta_i(\boldsymbol{n}) = \Delta_i(\boldsymbol{n}^{eq}) + \sum_j \mathscr{L}_{ij} n_j^{neq}, \tag{2.3}$$

where $\mathscr{L}_{ij}$ are the matrix elements of the linearized collision operator, $n_j^{neq} = n_j - n_j^{eq}$ is the non-equilibrium distribution, and $\Delta_i(\boldsymbol{n}^{eq}) = 0$. Somewhat surprisingly, this simple evolution equation is second-order accurate in space and time. The numerical diffusion that usually accompanies a low-order grid-based method is eliminated by the relationship between the eigenvalues of the linearized collision operator and the fluid viscosity (see for example, § 5 of Ladd & Verberg 2001).

The standard 19 velocity model comprises stationary particles and the 18 velocities corresponding to the [100] and [110] directions of a simple cubic lattice. The population density associated with each velocity has a weight a^{c_i} that describes the fraction of particles with velocity $\boldsymbol{c}_i$ in a system at rest; these weights depend only on the speed c_i and are normalized so that $\sum_i a^{c_i} = 1$. In order for the viscous stresses to be independent of direction, we require the rest density of particles in the [100] directions to be twice that of particles moving in the [110] directions. The optimum choice of weights for this model is

$$a^0 = \tfrac{1}{3}, \quad a^1 = \tfrac{1}{18}, \quad a^{\sqrt{2}} = \tfrac{1}{36}. \tag{2.4}$$

In our suspension simulations we use a three-parameter collision operator, allowing for separate relaxation of the five shear modes, one bulk mode, and nine kinetic modes. The post-collision distribution $n_i^\star = n_i + \Delta_i$ is written as

$$n_i^\star = a^{c_i} \left(\rho + \frac{\boldsymbol{j} \cdot \boldsymbol{c}_i}{c_s^2} + \frac{(\rho \boldsymbol{u}\boldsymbol{u} + \boldsymbol{\Pi}^{neq,\star}) : (\boldsymbol{c}_i \boldsymbol{c}_i - c_s^2 \mathbf{1})}{2c_s^4} \right), \tag{2.5}$$

where the sound speed $c_s = \Delta x / \sqrt{3} \Delta t$, Δx is the spacing between neighbouring fluid nodes and Δt is the time step. The non-equilibrium momentum flux $\boldsymbol{\Pi}^{neq} = \sum_i n_i^{neq} \boldsymbol{c}_i \boldsymbol{c}_i$ relaxes owing to collisions at the lattice nodes,

$$\boldsymbol{\Pi}^{neq,\star} = (1 + \lambda) \overline{\boldsymbol{\Pi}}^{neq} + \tfrac{1}{3}(1 + \lambda_v)(\boldsymbol{\Pi}^{neq} : \mathbf{1})\mathbf{1}, \tag{2.6}$$

where $\boldsymbol{\Pi}^{neq} = \boldsymbol{\Pi} - \boldsymbol{\Pi}^{eq}$ and $\boldsymbol{\Pi}^{eq} = \rho c_s^2 + \rho \boldsymbol{u}\boldsymbol{u}$ is the equilibrium momentum flux. The parameters λ and λ_v are eigenvalues of the linearized collision operator and are related to the fluid shear and bulk viscosities:

$$\eta = -\rho c_s^2 \Delta t \left(\frac{1}{\lambda} + \frac{1}{2} \right), \quad \eta_v = -\frac{2\rho c_s^2}{3} \Delta t \left(\frac{1}{\lambda_v} + \frac{1}{2} \right). \tag{2.7}$$

The factor of 1/2 serves to correct for numerical diffusion, so that viscous momentum diffuses at the expected speed for the given viscosity. For low-Reynolds-number flows, the most suitable values are $\lambda = \lambda_v = -1$ (Ladd & Verberg 2001).

In the presence of an externally imposed force density $\boldsymbol{f}_{ext}$, for example a pressure gradient or a gravitational field, the time evolution of the lattice-Boltzmann model

includes an additional contribution $f_i(\boldsymbol{r}, t)$,

$$n_i(\boldsymbol{r} + \boldsymbol{c}_i \Delta t, t + \Delta t) = n_i(\boldsymbol{r}, t) + \Delta_i [\boldsymbol{n}(\boldsymbol{r}, t)] + f_i(\boldsymbol{r}, t). \tag{2.8}$$

This forcing term can also be expanded in a power series in the velocity,

$$f_i = a^{c_i} \left[\frac{\boldsymbol{f}_{ext} \cdot \boldsymbol{c}_i}{c_s^2} + \frac{(\boldsymbol{u}\boldsymbol{f}_{ext} + \boldsymbol{f}_{ext}\boldsymbol{u}) : (\boldsymbol{c}_i \boldsymbol{c}_i - c_s^2 \mathbf{1})}{2c_s^4} \right] \Delta t. \tag{2.9}$$

More accurate solutions to the velocity field are obtained if it includes a portion of the momentum added to each node (Ladd & Verberg 2001),

$$\boldsymbol{j}' = \rho \boldsymbol{u}' = \sum_i n_i \boldsymbol{c}_i + \tfrac{1}{2} \boldsymbol{f}_{ext} \Delta t. \tag{2.10}$$

The macrodynamical behaviour arising from the lattice-Boltzmann equation can be found from a multi-scale analysis (Frisch *et al.* 1987), using an expansion parameter ϵ, defined as the ratio of the lattice spacing to a characteristic macroscopic length; the hydrodynamic limit corresponds to $\epsilon \ll 1$. It can be shown that the lattice-Boltzmann equation reproduces the Navier–Stokes equations with corrections that are of the order u^2 and ϵ^2 (Ladd & Verberg 2001). Thus, at sufficiently low Mach numbers, the method is second-order accurate in space, with relative errors proportional to Δx^2. It is also second-order accurate in time if the viscosities are defined according to (2.7).

2.2. *Particle suspensions*

Boundary conditions in the lattice-Boltzmann model are straightforward to implement, even for non-planar surfaces (Ladd 1994*a*). Solid particles are defined by a surface, which cuts some of the links between lattice nodes. Fluid particles moving along these links interact with the solid surface at boundary nodes placed halfway along the links. Thus we obtain a discrete representation of the particle surface, which becomes more and more precise as the particle becomes larger (figure 1). The moving boundary condition (Ladd 1994*a*) without interior fluid (Aidun, Lu & Ding 1998) is then implemented as follows. We take the set of fluid nodes $\boldsymbol{r}$ just outside the particle surface, and for each node all the velocities $\boldsymbol{c}_b$ such that $\boldsymbol{r} + \boldsymbol{c}_b \Delta t$ lies inside the particle surface. An example of a set of boundary-node velocities is shown by the arrows in figure 1. Each of the corresponding population densities is then updated according to a simple rule which takes into account the motion of the particle surface (Ladd 1994*a*);

$$n_{b'}(\boldsymbol{r}, t + \Delta t) = n_b^*(\boldsymbol{r}, t) - \frac{2a^{c_b} \rho_0 \boldsymbol{u}_b \cdot \boldsymbol{c}_b}{c_s^2}, \tag{2.11}$$

where $n_b^*(\boldsymbol{r}, t)$ is the post-collision distribution at $(\boldsymbol{r}, t)$ in the direction $\boldsymbol{c}_b$, and $\boldsymbol{c}_{b'} = -\boldsymbol{c}_b$. The local velocity of the particle surface,

$$\boldsymbol{u}_b = \boldsymbol{U} + \boldsymbol{\Omega} \times (\boldsymbol{r}_b - \boldsymbol{R}), \tag{2.12}$$

is determined by the particle velocity $\boldsymbol{U}$, angular velocity $\boldsymbol{\Omega}$, and centre of mass $\boldsymbol{R}$; $\boldsymbol{r}_b = \boldsymbol{r} + \boldsymbol{c}_b \Delta t/2$ is the location of the boundary node.

As a result of the boundary node updates, momentum is exchanged locally between the fluid and the solid particle, but the combined momentum of solid and fluid is conserved. The forces exerted at the boundary nodes can be calculated from the momentum transfer during the boundary-node update (equation (2.11)),

$$\boldsymbol{f}_b\left(\boldsymbol{r}_b, t + \tfrac{1}{2}\Delta t\right) = \frac{\Delta x^3}{\Delta t} \left[2n_b^*(\boldsymbol{r}, t) - \frac{2a^{c_b} \rho_0 \boldsymbol{u}_b \cdot \boldsymbol{c}_b}{c_s^2} \right] \boldsymbol{c}_b. \tag{2.13}$$

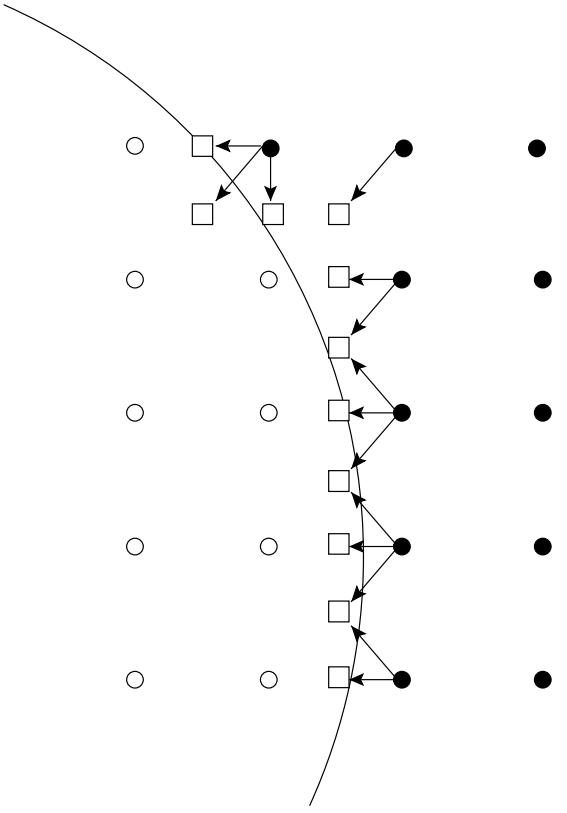

FIGURE 1. Location of boundary nodes along a curved surface. The incoming velocities along links cutting the boundary surface are indicated by arrows. The locations of the boundary nodes are shown by open squares, and the fluid nodes by solid circles. The particles used in the majority of the simulations have a radius of $2\Delta x$, or about half the linear resolution of the object sketched here.

The particle forces $\boldsymbol{F}$ and torques $\boldsymbol{T}$ are then obtained by summing $\boldsymbol{f}_b(\boldsymbol{r}_b)$ and $\boldsymbol{r}_b \times \boldsymbol{f}_b(\boldsymbol{r}_b)$ over all the boundary nodes associated with a particular particle. It can be shown analytically that the force on a planar wall in a linear shear flow is exact (Ladd 1994*a*), and several numerical examples of lattice-Boltzmann simulations of hydrodynamic interactions are given in Ladd (1994*b*). For pairs of particles near contact, an additional lubrication force is added to correct for the missing singular interactions (Nguyen & Ladd 2002).

An implicit update of the particle velocities is used to ensure stability (Lowe, Frenkel & Masters 1995). The particle force and torque are separated into a component that depends on the incoming velocity distribution and a component that depends, via $\boldsymbol{u}_b$, on the particle velocity and angular velocity (equations (2.12) and (2.13));

$$\boldsymbol{F} = \boldsymbol{F}_0 - \boldsymbol{\zeta}^{\mathrm{FU}} \cdot \boldsymbol{U} - \boldsymbol{\zeta}^{\mathrm{F}\Omega} \cdot \boldsymbol{\Omega}, \tag{2.14}$$

with a similar equation for the torque. The velocity independent forces are determined at the half-time step,

$$\boldsymbol{F}_0\left(t + \tfrac{1}{2}\Delta t\right) = \frac{\Delta x^3}{\Delta t} \sum_b 2 n_b^*(\boldsymbol{r}, t) \boldsymbol{c}_b, \tag{2.15}$$

where the sum is over all the boundary nodes, b, describing the particle surface. The matrices

$$\boldsymbol{\zeta}^{\mathrm{FU}} = \frac{2\rho_0 \Delta x^3}{c_s^2 \Delta t} \sum_b a^{c_b} \boldsymbol{c}_b \boldsymbol{c}_b, \tag{2.16}$$

$$\boldsymbol{\zeta}^{\mathrm{F}\Omega} = \frac{2\rho_0 \Delta x^3}{c_s^2 \Delta t} \sum_b a^{c_b} \boldsymbol{c}_b (\boldsymbol{r}_b \times \boldsymbol{c}_b), \tag{2.17}$$

are high-frequency friction coefficients, and describe the instantaneous force on a particle in response to a sudden change in velocity. There are corresponding equations for the friction coefficients associated with the torque. An implicit update of the particle velocities requires two passes through the boundary nodes. On the first pass, the population densities are used to calculate $\boldsymbol{F}_0$ and $\boldsymbol{T}_0$. The equations of motion for the particle velocities reduce to linear ordinary differential equations, and are solved by the implicit Euler method. These velocities are then used to calculate the new population densities in a second sweep through the boundary nodes.

The lubrication forces complicate the update of the particle velocity because they involve interactions between many particles, especially at higher concentrations. Since a many-particle implicit update can lead to large linear systems of equations, we have implemented an algorithm which uses an implicit update only where necessary. Schematically, we solve the coupled differential equations

$$\dot{\boldsymbol{x}} = -\boldsymbol{A} \cdot \boldsymbol{x} + \boldsymbol{b} \tag{2.18}$$

by splitting the matrix $\boldsymbol{A}$ into regular $\boldsymbol{A}^R$ and singular $\boldsymbol{A}^S$ components, $\boldsymbol{A} = \boldsymbol{A}^R + \boldsymbol{A}^S$. $\boldsymbol{A}^S$ contains only the most strongly diverging friction coefficients of pairs of particles very near contact. Using a mixed explicit–implicit differencing,

$$\frac{\boldsymbol{x}(t+\Delta t) - \boldsymbol{x}(t)}{\Delta t} = -\boldsymbol{A}^R \cdot \boldsymbol{x}(t) - \boldsymbol{A}^S \cdot \boldsymbol{x}(t+\Delta t) + \boldsymbol{b}, \tag{2.19}$$

we obtain the first-order update

$$(\boldsymbol{1} + \boldsymbol{A}^S \Delta t) \cdot \boldsymbol{x}(t+\Delta t) = \boldsymbol{x}(t) - \boldsymbol{A}^R \Delta t \cdot \boldsymbol{x}(t) + \boldsymbol{b} \Delta t. \tag{2.20}$$

The important point is that, by a suitable relabelling of the particle indices, $\boldsymbol{A}^S$ can be cast into a block diagonal form, with the potential for an enormous reduction in the computation time for the matrix inversion. The relabelling is achieved by a cluster analysis; the details are given in Nguyen & Ladd (2002).

The implicit update becomes impractical in the dense pack at the base of a settling suspension. In this region, clusters of particles in close contact span the container dimensions and quickly exceed the limit where the linear system solve is a small component of the total computational cost, typically at about 2000 particles per cluster. Since the particle velocities are very small in this region, we define a front below which the particle velocities are set to zero. The front is set to the plane where the particle volume fraction first exceeds a preset value, typically 50%. In practice, the front is well below the sediment–suspension interface.

2.3. *Settling of pairs of particles*

The algorithm for simulating the hydrodynamic interactions between suspended particles, described in §§2.1 and 2.2, has been extensively tested by comparisons with theory, independent simulations and experiment (Ladd 1994*b*; Nguyen & Ladd 2002). However, in dynamic simulations, artefacts introduced by the motion of the particle

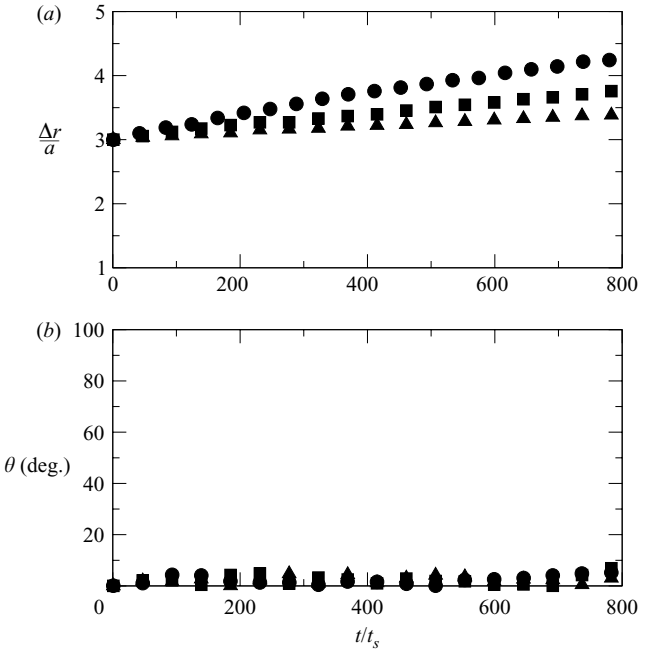

FIGURE 2. Settling of a horizontal pair of particles at different Reynolds numbers; $Re = 0.1$ (circles), 0.05 (squares), 0.025 (triangles). The centre–centre separation, Δr, and orientation to the horizontal, θ (in degrees), are plotted as a function of time; $t_s = a/U_0$ is the Stokes time. The simulations used particles of radius $a = 2\Delta x$ in a periodic box $10a \times 10a \times 40a$.

over the grid can cause additional errors in the trajectories of the particles. We have previously found (Nguyen & Ladd 2002) that fluctuations in particle velocity are of the order of one per cent for particles of the size used in this work. More sophisticated boundary conditions (Bouzidi, Firdaouss & Lallemand 2001; Verberg & Ladd 2001; Ginzbourg & d'Humières 2003; Rohde *et al.* 2003) reduce the fluctuations by at least an order of magnitude, but none of these ideas has yet been implemented in a multi-particle simulation. Here we examine the settling of pairs of particles to assess the effects of grid artefacts and the residual fluid inertia.

Two spheres settling side-by-side repel each other when the spacing is of the order of the particle diameter (Jayaweera, Mason & Slack 1964; Kim, Elghobashi & Sirignano 1993). The rotation of the particles gives rise to a lift force, which tends to drive them apart. At small Reynolds numbers, $Re < 0.1$, the repulsion between the particles become negligible and the separation distance does not change appreciably over time (Wu & Manasseh 1998). We examined the settling of two particles at a range of particle Reynolds numbers $0.025 < Re < 0.1$, where the Reynolds number, $Re = 2\rho\langle U_\parallel\rangle a/\eta$, is given in terms of the mean settling velocity $\langle U_\parallel\rangle$, particle diameter $2a$, fluid density ρ and viscosity η. Figure 2 shows that the particles maintain their orientation, and slowly drift apart with a velocity proportional to Re. At the highest Reynolds number, the separation velocity is about 0.15% of the settling velocity, not inconsistent with the experiments of Wu & Manasseh (1998), which were for shorter times, of the order of $150t_s$, and touching particles $\Delta r/a = 2$.

Figure 3 shows the relative motion of a pair of particles settling with different initial orientations. Particles oriented in the horizontal ($\theta = 0$) and vertical ($\theta = 90^\circ$) directions maintain their initial orientations over time, although the particles drift away

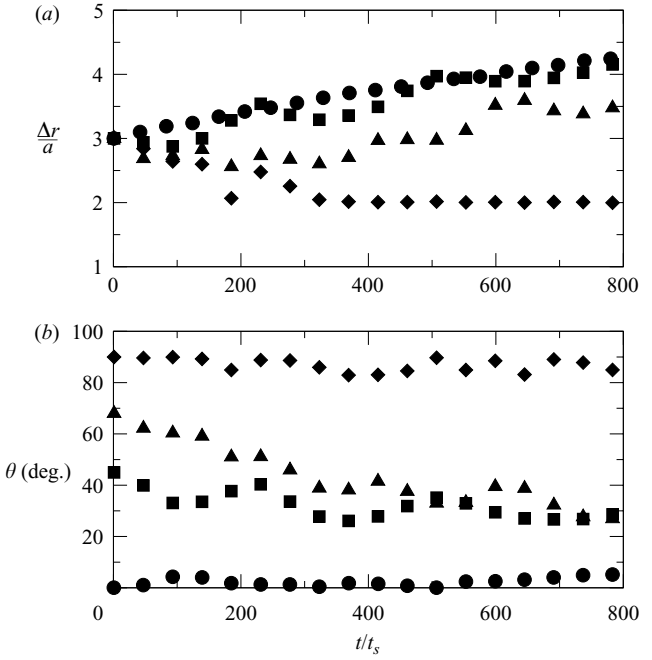

FIGURE 3. Settling of a pair of particles at various orientations: $\theta = 0°$ (circles), 45° (squares), 68° (triangles), 90° (diamonds). The centre–centre separation, Δr, and orientation to the horizontal, θ (in degrees), are plotted as a function of time. The Reynolds number $Re = 0.1$ in each case.

from each other (horizontal) or towards each other (vertical), owing to the residual fluid inertia. In Stokes flow ($Re = 0$), a pair of spherical particles oriented at some intermediate angle should settle as a unit, maintaining the separation and orientation of the pair, but in our simulations particles at off-axis orientations have slightly different velocities and the pair slowly rotates with time. Nevertheless, the variations in particle velocity are much smaller than the effects of polydispersity, which is inherent in laboratory experiments. Similar variations in velocity would be produced by polydispersity of the order of 0.1%, whereas in most laboratory experiments the polydispersity is 1–10%.

2.4. *Sedimentation simulations*

Simulations of sedimentation are computationally demanding because of the large number of particles necessary to capture the length scales involved in the development of hydrodynamic interactions. The simulation parameters are therefore a carefully chosen compromise between several competing factors, limited by the requirement that a calculation be completed in a reasonable amount of time, of the order of one month. Experiments (Segré *et al.* 1997) suggest that the characteristic length scale is the mean interparticle spacing $d = a\phi^{-1/3}$ and that the screening length is of the order of $20d$. The computational time required for our simulations is, to a first approximation, proportional to the number of fluid grid points, and therefore the total volume is an important limitation. We have limited our calculations to a single volume fraction $\phi = 0.13$ ($d \approx 2a$), which was chosen as a reasonable compromise between keeping d small and avoiding the additional complications of a highly concentrated suspension. We used a cell with a square cross-section, and studied a range of widths from $W = 8d$ to $W = 24d$. Laboratory experiments use larger cells, $100 < W/a < 1000$, but smaller

volume fractions, so that W/d is usually less than 100 (Segré *et al.* 1997; Bernard-Michel *et al.* 2002), although larger cells are sometimes used (Guazzelli 2001; Tee *et al.* 2002). In most instances, the simulation cells were bounded at the top and bottom by rigid impermeable walls and we have found by experience that a cell height $H = 1000a \approx 500d$ is necessary to allow time for the suspension to reach a steady state. We have varied the cell height in some instances, as reported in § 3.2. At the chosen volume fraction, the suspension contains between 8000 and 72000 solid particles.

A key component of this work is the assessment of the effects of boundary conditions on the suspension microstructure and dynamics. A no-slip boundary breaks the macroscopic translational invariance in the direction normal to the boundary surface, and because of the long-range character of hydrodynamic interactions, this symmetry breaking may have a significant effect far from the boundary. We have therefore compared results for three different sets of boundary conditions: systems bounded in all directions by rigid walls, which we denote as 'Box'; systems bounded by walls at the top and bottom, while the vertical faces were periodic ('Bounded'); and systems with periodic boundary conditions on all faces ('PBC'). For systems with periodic boundaries on all faces, the height to width ratio was set to 4:1, as previous work showed no change occurred with taller cells (Ladd 1997). In the simulations with no-slip boundaries at the top and bottom ('Box' and 'Bounded'), data were taken in a window, typically of height $200a$, centred around $350a$ from the bottom of the vessel, as is typical in experimental measurements. We have checked that the results are insensitive to the position of the viewing window as long as it is located in a region of uniform particle concentration. Fully periodic systems ('PBC') are spatially homogeneous, and data are averaged over the entire volume in this case. When considering the system dimensions, it should be noted that an extra $2a$ has been added to all dimensions bounded by no-slip walls. This allows for the excluded volume of the walls and keeps the particle volume fraction as close as possible to 13%. We will identify the system dimensions in this paper without the additional excluded volume correction.

A particle radius of two grid spacings, $a = 2\Delta x$, was used in all these simulations, as compared with $a = 1.5\Delta x$ or $a = 1.25\Delta x$ in previous work (Ladd 1997, 2002). Test calculations with small numbers of particles (see § 3.3) suggest that there are no qualitative changes to the results if larger particles are used. The largest systems studied in this work contain 72 000 particles and approximately 20 million grid points. The simulations were run for 2000 Stokes times, where the Stokes time $t_s = a/U_0$ is the time it takes an isolated particle to settle one radius. The gravitational force was set so that the Stokes time corresponded to 250 time steps and the complete settling simulation therefore required half a million steps. The lengthiest calculations take about 1 month on a cluster of 8 Pentium 4 processors (2.4 GHz). The typical particle Reynolds number was $Re = 0.06$, whereas in laboratory experiments it is usually one to two orders of magnitude smaller. Although the residual inertia is a potential source of complication, tests described in § 3.3 and laboratory experiments (Cowan, Page & Weitz 2000) suggest that inertial effects are small at Reynolds numbers $Re < 1$.

3. Velocity fluctuations

We have examined the transient and steady-state fluctuations in particle velocity under different macroscopic boundary conditions, in order to assess the effects of container size on the amplitude of the fluctuations. This issue has already been examined from several different perspectives (see § 1); here we present a complete and up-to-date account of our own investigations.

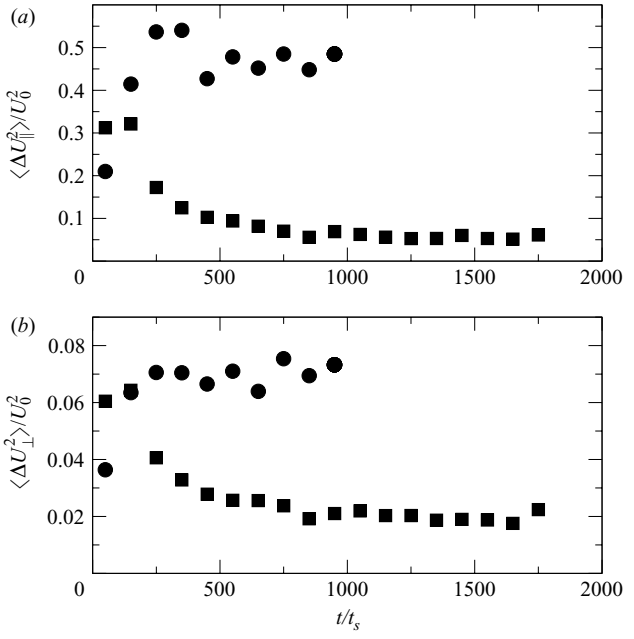

FIGURE 4. Particle velocity fluctuations as a function of time. (*a*) The vertical (‖) and (*b*) horizontal (⊥) fluctuations about the mean are shown for monodisperse suspensions of width $W = 48a$, bounded by rigid no-slip walls (circles) and periodic boundaries (squares). The sampling window for the box system was $250 \leqslant z/a \leqslant 400$ and the height of the cell was $1000a$.

3.1. *Time-dependent velocity fluctuations*

The initial particle configuration was sampled from the most-probable (or maximum entropy) distribution of hard spheres, which was generated by a Monte-Carlo simulation. At moderate concentrations, particle positions are correlated because of excluded volume. Thus the initial distribution does not obey Poisson statistics, but the pair probability is nevertheless random for separations of more than 5–10 particle radii. The particle velocities were initialized by a run of $200t_s$ during which time the particle positions were fixed in place, although the velocities were free to adapt to the local flow. Thus the initial configuration for the dynamical simulation ($t = 0$) was an idealized well-stirred distribution, without large-scale spatial inhomogeneities.

Simulations have shown that the time evolution of the velocity fluctuations depends qualitatively on the macroscopic boundary conditions (Ladd 2002). Figure 4 illustrates the different time dependence for 'PBC' and 'Box' geometries. With periodic boundary conditions the velocity fluctuations initially increase with time, reaching a plateau after approximately $200t_s$ (Ladd 1993, 1997). However, when the container is bounded by no-slip walls, the fluctuations decay with time, over a period of approximately $1000t_s$. The initial fluctuations are comparable to a homogeneous suspension ('PBC'), but in the 'Box' geometry, they decay to a much smaller value. A similar decay in the velocity fluctuations has been observed experimentally (Guazzelli 2001; Bernard-Michel *et al.* 2002).

The data in figure 5 show that velocity fluctuations decay to similar levels in both 'Box' and 'Bounded' geometries, and therefore the amplitude of the velocity fluctuations is controlled by the boundary conditions at the top and bottom of the container (Ladd 2002). As an additional test, we ran simulations with no-slip vertical walls

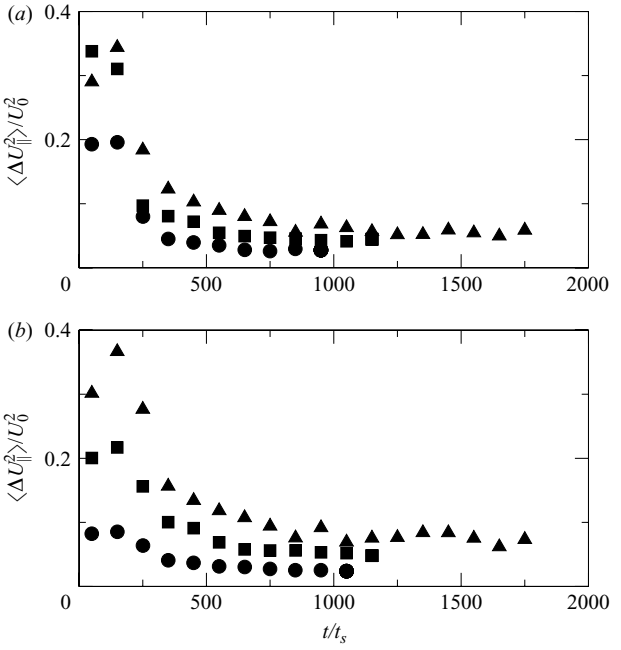

FIGURE 5. Particle velocity fluctuations as a function of time for (*a*) 'Box' and (*b*) 'Bounded' geometries. The vertical (||) fluctuations about the mean are shown for various widths: $W/a = 16$ (circles), 32 (squares) and 48 (triangles), respectively. Data were taken within a window $250 \leqslant z/a \leqslant 400$; the height of the cell was $1000a$.

and periodic boundary conditions at the top and bottom; these results were similar to the fully periodic case. Vertical no-slip boundaries may play an important role in containers with large aspect ratios (Brenner 1999), but our results show that there is no qualitative effect in containers with a square cross-section.

The decay of the velocity fluctuations in the bulk of the suspension cannot be explained by direct screening of the long-range interactions by the boundaries. Although a no-slip boundary does screen the hydrodynamic interactions of particles near the boundary, the screening does not extend to particles that are further from the wall than they are from each other (Brenner 1999). Thus in the measurement window, which is typically 5–10W from the container base, the hydrodynamic interactions are not significantly affected by the boundaries. Moreover, the time-dependent decay of the fluctuations suggests that there is a redistribution of the particle configurations during the settling process. The most likely mechanism is that the container bottom and the suspension–supernatant interface act as sinks of fluctuation energy, as suggested by Hinch (1988). A horizontal density fluctuation can be idealized as two regions (or blobs) side by side, one slightly heavier than the average and the other slightly lighter. These density fluctuations convect to one of the two interfaces and are absorbed by the density gradient at the interface. Scaling arguments suggest that a horizontal density fluctuation of length l convects with a velocity $v_l \approx U_0(\phi l/a)^{1/2}$ with respect to the mean (Hinch 1988), so that fluctuations drain away on a time scale

$$t_C(l) \approx l/v_l \approx (l/a\phi)^{1/2} t_s. \tag{3.1}$$

In the absence of no-slip boundaries at the top and bottom of the container, large-scale density fluctuations recirculate through the suspension, and the fluctuations in density and velocity are therefore time independent, as shown in figure 4.

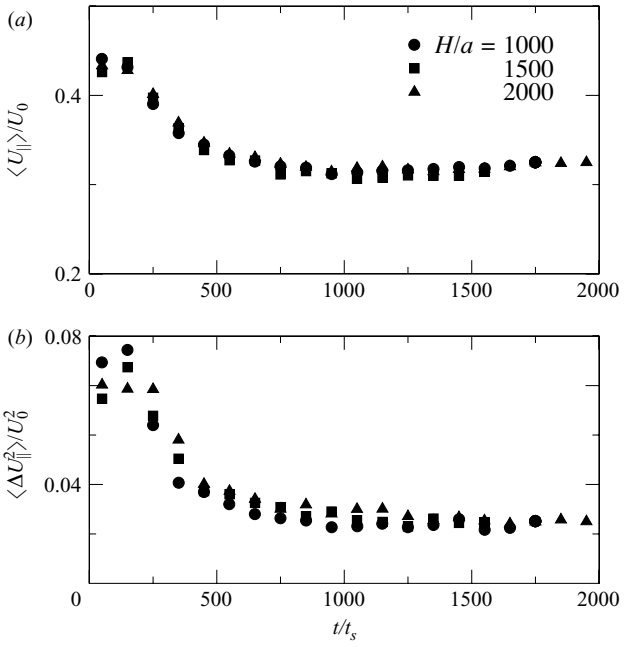

FIGURE 6. Mean settling velocity, $\langle U_\parallel \rangle$, and fluctuations in settling velocity, $\langle \Delta U_\parallel^2 \rangle$, as a function of time for different system heights, H. The observation window is located between $300 \leqslant z/a \leqslant 500$ in all cases. The data are taken in a 'Bounded' geometry of width $W/a = 16$.

To account for the velocity fluctuations reaching steady state, the model must include some mechanism for replenishing the large-scale density fluctuations; otherwise the velocity fluctuations will continually decrease. We will assume that small-scale (of order d) density fluctuations are generated by conversion of gravitational potential energy, and then spread out by hydrodynamic diffusion, resulting from short-range multi-particle interactions. The characteristic length of the density fluctuation will grow to order l in a time of order

$$t_D(l) \approx l^2/D, \tag{3.2}$$

where $D_\parallel \approx U_0 a$ is the hydrodynamic dispersion coefficient. By balancing the convection time, t_C, with the diffusion time, t_D, we obtain a critical length scale, $l_c \approx a\phi^{-1/3}$, beyond which fluctuations drain away more rapidly than they can be replenished by diffusion. Thus the system reaches a steady state with a correlation length that is independent of system width and proportional to the mean interparticle spacing $a\phi^{-1/3}$, as observed experimentally (Segré *et al.* 1997; Guazzelli 2001). This is the physical idea underlying the convection–diffusion model proposed by Levine *et al.* (1998), which will be discussed in detail in §4.2. An alternative explanation, based on the development of a stratified density profile in the suspension (Mucha & Brenner 2003; Mucha *et al.* 2004), will be discussed in §§4.1 and 5.4. The scaling of the diffusivity used here, $D \sim U_0 a$, is consistent with the idea of a 'bare' diffusivity that is renormalized by long-wavelength fluctuations (Levine *et al.* 1998), but not with the model proposed by Mucha & Brenner (2003).

Within a viewing window far from the sediment and supernatant interfaces, the velocity fluctuations reach a quasi-steady state after a time period of the order of $1000t_s$. The mean settling velocity and the velocity fluctuations within the viewing window are unaffected by system height, as shown in figure 6. For the height used in most of

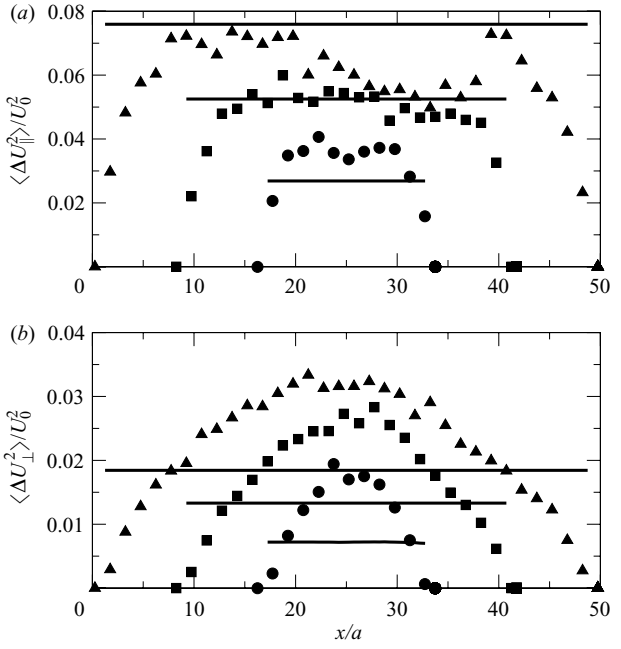

FIGURE 7. Particle velocity fluctuations at steady state. Profiles are shown for the 'Box' system (solid symbols) at different widths: $W/a = 16$ (circles), 32 (squares) and 48 (triangles). The profile is taken within a central slice of the viewing window of thickness $2a$, comparable to particle-image-velocimetry experiments. The solid lines indicate results for the 'Bounded' geometry, averaged over the whole cross-section. The temporal and spatial windows used for each system are given in table 1.

our simulations ($H = 1000a$), there is an upper time limit to the simulations of about $1500t_s$, before the supernatant interface starts to interfere with the measurements in the viewing window. The time taken to reach steady state depends on the container width (see figure 5), ranging from 600 to $700t_s$ for the smallest systems ($W = 16a$) to about $1000t_s$ for the largest systems ($W = 48a$).

3.2. *Steady-state settling*

A settling particle produces a disturbance in the fluid flow that decays as r^{-1} at low Reynolds number, where r is the distance from the disturbance. This disturbance causes a fluctuation in the velocity of another particle that decays as r^{-2}. Assuming the particles are distributed uniformly, then integration over volume leads to the well-known result:

$$\langle U^2 \rangle \propto W, \tag{3.3}$$

where W is the container dimension (Caflisch & Luke 1985). Precise results have been worked out in the low-concentration limit for several different geometries (Ladd 1993; Koch 1994; Mucha *et al.* 2004). The data in figure 5 show that the initial velocity fluctuations follow the Caflisch & Luke (1985) scaling (equation (3.3)), while the steady-state velocity fluctuations grow more slowly with system size.

The steady-state fluctuations across the viewing window are shown in figure 7. The time window for averaging was determined separately for each system, depending on the time to reach a quasi-steady state (see figure 5); the duration of the time window was $400t_s$ in all cases. The results were also averaged over a range of vertical positions,

	W/a	Box	Centre	Bounded		Time (t_s)	Space (a)
$\langle \Delta U_{\parallel}^2 \rangle / \langle U_{\parallel} \rangle^2$	16	0.22	0.27	0.29	Box	600–1000	150–550
	32	0.37	0.47	0.55		800–1200	200–500
	48	0.47	0.52	0.73		1100–1500	250–450
$\langle \Delta U_{\perp}^2 \rangle / \langle U_{\parallel} \rangle^2$	16	0.07	0.15	0.08	Bounded	700–1100	200–650
	32	0.12	0.23	0.14		800–1200	250–600
	48	0.17	0.28	0.18		1000–1400	250–500

TABLE 1. Steady-state particle velocity fluctuations in a monodisperse suspension as a function of system width. Fluctuations have been averaged over the whole cross-section in the columns labelled 'Box' and 'Bounded'. The column labelled 'Centre' is the value along the centreline in the 'Box' geometry (figure 7), and is most closely related to experimental measurements. The temporal and spatial windows used for averaging are shown in the last two columns.

chosen so that the density and velocity fluctuations were constant apart from statistical errors (see figure 18). The spatial and temporal windows used in figure 7 are given in table 1. For the 'Bounded' geometry the velocity fluctuations were averaged over the whole horizontal plane, while for the 'Box' geometry the fluctuations were measured in a thin slice of width $2a$ located in the centre of the container. Figure 7 shows that even though the velocity fluctuations grow less than linearly with width, they do not converge to a width-independent value for the range of system sizes studied.

The steady-state velocity fluctuations are summarized in table 1. Results for the 'Box' geometry were averaged in two different ways; over the whole horizontal plane and along the centreline of the system (the central region in figure 7). The data calculated along the centreline were obtained from the small number of particles in a cross-section of area $4a^2$; it has large statistical errors, but is more closely related to experimental measurements than the average over the plane. Results for the 'Bounded' geometry were averaged over the horizontal plane only, since the system is homogeneous in that plane. The results show similar trends with increasing system size, although the 'Bounded' geometry is less saturated than the 'Box' geometry. The anisotropy in the vertical and horizontal fluctuations is noticeably less in the 'Box' geometry than the typical experimental measurement $\langle \Delta U_{\parallel}^2 \rangle = 4 \langle \Delta U_{\perp}^2 \rangle$, but in § 5.2 it will be shown that the calculated anisotropy is increased by polydispersity in the particle size.

Figure 8 shows that the simulation data agree quite well with experimental measurements if the container width, W, is scaled by the mean interparticle separation, $d = a\phi^{-1/3}$. It has been shown experimentally that d is the characteristic length scale describing the effect of particle concentration (Segré *et al.* 1997; Bernard-Michel *et al.* 2002); the measured correlation length is always of the order of $20d$, regardless of concentration. The data in figure 8 indicate that larger containers are required for the velocity fluctuations to fully saturate and become independent of system size, but this is not computationally feasible at present. The simulation results averaged over the horizontal plane are about 20% smaller than experimental measurements, while values at the centreline are closer to experiment, but the statistics are poor. It should be noted that in using the empirical fit to experimental data in figure 8,

$$\left.\begin{aligned} \langle \Delta U_{\parallel}^2 \rangle^{1/2} &= 2 \langle U_{\parallel} \rangle \phi^{1/3} \left(1 - \mathrm{e}^{-6W/d}\right), \\ \langle \Delta U_{\perp}^2 \rangle^{1/2} &= \langle U_{\parallel} \rangle \phi^{1/3} \left(1 - \mathrm{e}^{-6W/d}\right); \end{aligned}\right\} \tag{3.4}$$

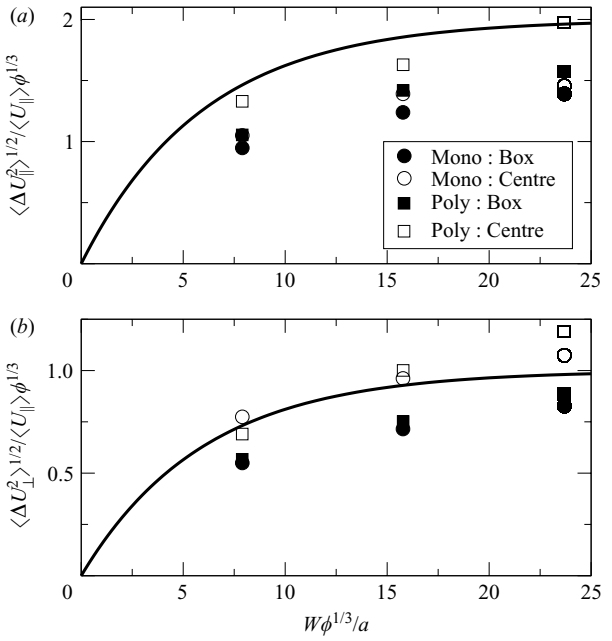

FIGURE 8. Comparison of steady-state particle velocity fluctuations with experimental results. Simulation results for monodisperse suspensions (circles) and polydisperse (see § 5.2) suspensions (squares) are plotted against the ratio of the cell size to the mean interparticle spacing, $W/a\phi^{1/3}$. The 'Box' geometry has been used to compare with a fit to experimental data given by Segré *et al.* (1997) (equation (3.4)), shown by the solid line . The column labelled 'Centre' is the value along the centreline, and is most closely related to experimental measurements.

we have taken the smallest container dimension as the controlling length, whereas Segré *et al.* (1997) used the larger lateral dimension in fitting their experiments. They claimed a better fit from this choice, but it cannot be justified physically or theoretically.

3.3. *Numerical errors*

The simulations described in this paper are not expected to be a completely quantitative description of Stokes-flow hydrodynamics. In particular, we cannot disregard the possibility that inertial effects play a role on scales larger than the particle radius. At the volume fraction used in this work, we can expect that particle velocity correlations persist for distances of the order of $40a$ (Segré *et al.* 1997), and the Reynolds number based on this distance is 1.2. The data in figure 9 show that, in a system of width $W = 16a$ ($N = 8000$), inertia plays no role for particle Reynolds numbers $Re < 0.1$; the Reynolds number based on container width, $Re_W = \rho\langle U_{\parallel}\rangle W/\eta$, ranges from 0.12 to 0.96. We have verified this conclusion in a larger system as well ($W = 32a$, $N = 32\,000$); no significant difference in velocity fluctuations was observed between $Re = 0.06$ and 0.03 ($Re_W = 0.96$ and 0.48). Computational limitations prevented a study of the effects of inertia in still larger systems, but the largest value of Re_W is only 1.44. Experimental results (Cowan *et al.* 2000) suggest inertial effects are small if $Re < 1$, a much weaker condition.

An additional concern with lattice-Boltzmann simulations are artefacts introduced by the motion of particles across the grid. It was shown in § 2.3 that these grid artefacts cause a small but measurable dispersion in the trajectories of pairs of particles, and

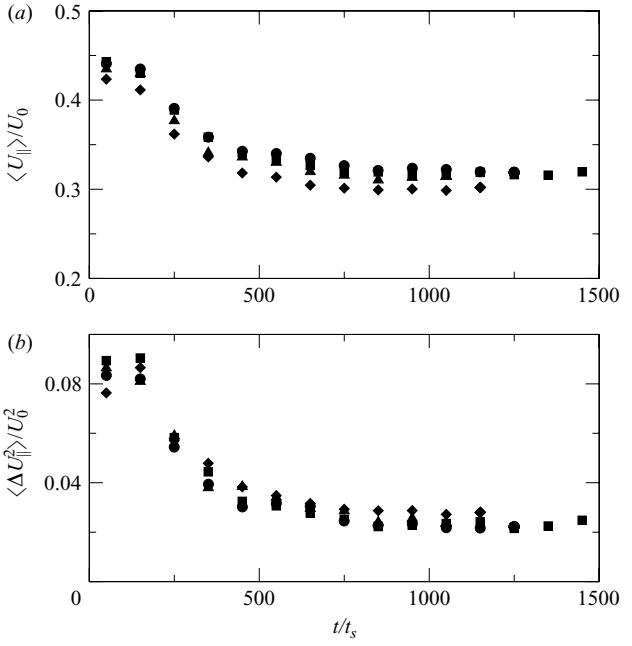

FIGURE 9. Effect of inertia on the mean settling velocity and fluctuations in settling velocity. The data are averaged within a window of height $250 \leqslant z/a \leqslant 400$ in the 'Bounded' geometry ($N = 8000$) for different Reynolds numbers; $Re = 0.015$ (circles), 0.03 (squares), 0.06 (triangles), and 0.12 (diamonds).

the same random noise may serve to weaken the microstructural changes that lead to suppression of velocity fluctuations. However, simulations with larger particles, with smoother trajectories are not qualitatively different. The effects of grid resolution are shown in figure 10; the larger particles correspond to a more refined mesh.

4. Microstructure

The dynamics of suspensions at low Reynolds numbers are controlled by the distribution of particle positions, which is sufficient to determine the velocities at any instant of time. In a settling suspension, subtle shifts in the pair correlation function can have a dramatic effect on the macroscopic behaviour. Specifically, it has been established that the amplitude of the velocity fluctuations are largely determined by the structure factor (Ladd 1993), and in particular its low-k limiting behaviour:

$$\langle \Delta U^2 \rangle \propto \frac{U_0^2 \phi}{a} \int \frac{S(\boldsymbol{k})}{k^4} \, \mathrm{d}\boldsymbol{k}, \tag{4.1}$$

where $S(\boldsymbol{k})$ was defined in (1.1). Explicit expressions for the velocity fluctuations in suspensions with periodic boundary conditions are given in Koch (1994). The most important point is that the amplitude of $\langle \Delta U^2 \rangle$ is controlled by the low-k behaviour of S. If $S(k \to 0)$ is some non-zero constant, as is the case at equilibrium, then the velocity fluctuations are proportional to container size, but if $S(k \to 0)$ vanishes as k^2 or faster, the divergence is suppressed.

It has not been possible to measure the structure factor of a settling suspension of non-Brownian particles experimentally, since the particles are too large for light-scattering measurements. However, fluctuations in particle concentration have been

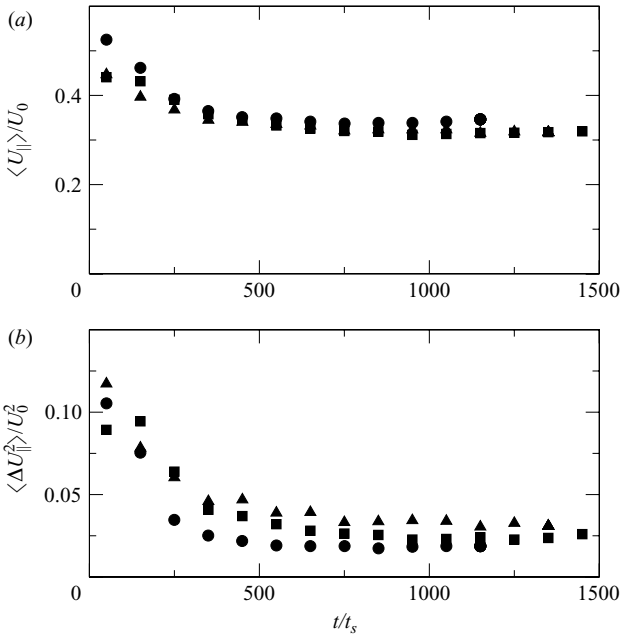

FIGURE 10. Effect of grid resolution on the mean settling velocity and fluctuations in settling velocity. The data are averaged within a window of height $250 \leqslant z/a \leqslant 400$ in the 'Bounded' geometry ($N = 8000$) for different particle sizes; $a = 1.25$ (circles), 2.0 (squares) and 2.7 (triangles).

measured within cylindrical and rectangular windows (Lei *et al.* 2001), but this gives only an angle average of the pair distribution. In numerical simulations, it is possible to calculate $S(\boldsymbol{k})$ as a function of both wavelength and direction. This is important, since some theories predict that the structure factor becomes highly anisotropic at long-wavelengths (Levine *et al.* 1998), with the horizontal fluctuations, $S(\boldsymbol{k}_\perp)$, vanishing as $k_\perp^2$ and the vertical fluctuations, $S(k_\parallel)$, remaining finite at all wavelengths. Here, we amplify on a preliminary report (Nguyen & Ladd 2004) of the structure factor in a steadily settling suspension, and investigate the possibility of stratification of the particle concentration (Mucha & Brenner 2003; Mucha *et al.* 2004).

4.1. *Particle concentration*

The interface between a settling suspension and the supernatant fluid is generally thought to be macroscopically sharp, owing to hindered settling (Davis & Hassen 1988). However, at low volume fractions, when hindered settling is negligible, hydrodynamic dispersion at the suspension–supernatant interface can lead to a stratification of the particle concentration and a non-uniform density in the bulk (Tee *et al.* 2002; Mucha & Brenner 2003; Mucha *et al.* 2004). The time evolution of the concentration profile, $\phi(z, t)$, can be approximated by a convection–diffusion equation, which, in a Lagrangian frame moving with the mean settling velocity $-U$, can be written as

$$\frac{\mathrm{d}\phi}{\mathrm{d}t} + U'\partial_z\phi = D_\parallel \partial_z^2 \phi, \tag{4.2}$$

where $U' = -\phi \mathrm{d}U/\mathrm{d}\phi$ is the velocity of a density perturbation with respect to the mean settling speed and $D_\parallel$ is the hydrodynamic diffusion coefficient in the vertical direction. If we take the diffusion coefficient measured in the largest 'Box' simulation,

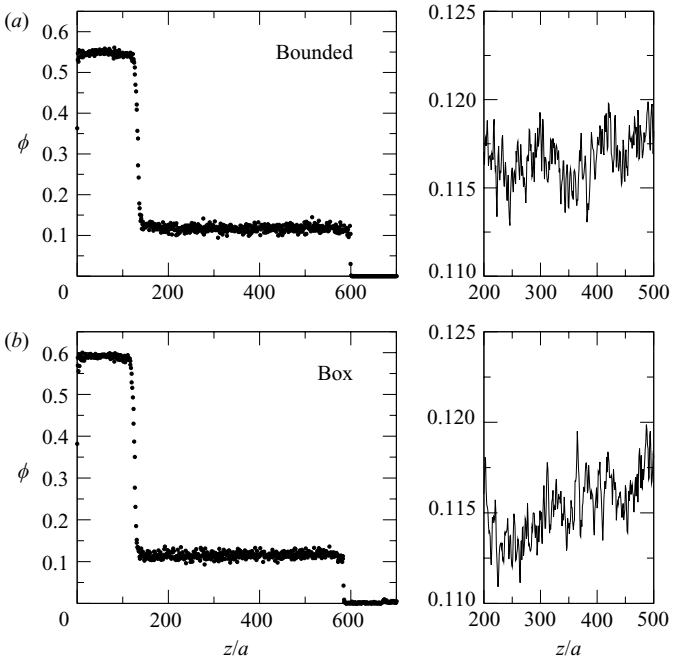

FIGURE 11. Particle volume fraction as a function of height, z. The dots indicate the instantaneous average over a horizontal slice of thickness a, at a time $t = 1200t_s$. The steady-state ($1000 < t/t_s < 1400$) density profile in the viewing window is shown in the adjacent plots. Results are shown for the (*a*) 'Box' and (*b*) 'Bounded' geometries for systems of width $W = 48a$ ($N = 72\,000$).

$D_\parallel = 4\langle U_\parallel \rangle a$, the solution to (4.2) is similar to the profiles shown in figure 11; in particular, there is a bulk region where the concentration is constant, and a sharp interface spread over approximately 10 particle diameters.

Stratification has been proposed as a mechanism for suppressing velocity fluctuations (Luke 2000), by making it possible for fluctuations in particle concentration to reach a neutrally buoyant position in the suspension without draining all the way to an interface. However, the density profiles for 'Bounded' and 'Box' geometries shown in figure 11 are not stratified; instead the concentration profile is uniform in the bulk and the suspension–supernatant interface is sharp. Hydrodynamic dispersion does cause a spreading of the interface, but this is compensated by hindered settling, which convects the less dense regions at a higher velocity than the high-density regions and thereby sets up a convective flux in opposition to the diffusive flux. Balancing the convective and diffusive concentration fluxes with respect to a frame moving with the mean settling velocity, we estimate an interface thickness, $D_\parallel / U'$ of the order of $5a$, at this volume fraction. The prediction of a sharp interface is consistent with the simulated density profile shown in figure 11.

The plots of average concentration shown in figure 11 have a positive slope in $\log \phi$ of the order of $10^{-4}a^{-1}$, while other simulations have negative slopes of comparable magnitude. This suggests that any residual density gradient must have a characteristic length considerably greater than $10^4 a$. Otherwise, a negative slope in $\log \phi$ would be consistently observed above the noise. We conclude that the stratification is most probably below the predicted critical stratification (Mucha *et al.* 2004), which is about $10^{-4}a^{-1}$ at this system size and volume fraction. Later, we will see that that the velocity

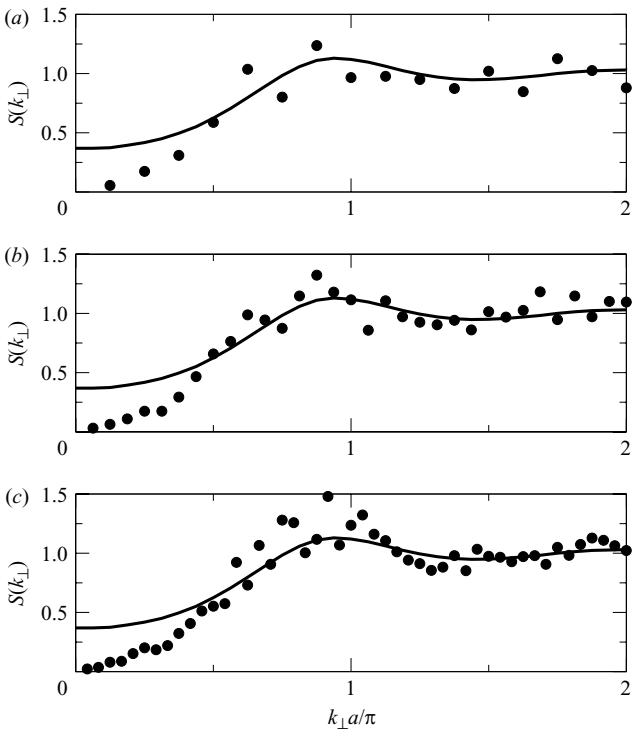

FIGURE 12. Structure factor describing horizontal density fluctuations, $S(k_\perp)$, for various system sizes: (*a*) $W = 16a$, (*b*) $32a$, and (*c*) $48a$. The data were averaged within the viewing window of the 'Bounded' geometry at steady state, and are essentially independent of system size for a given wavelength. The equilibrium structure factor is represented by the solid line.

fluctuations in monodisperse suspensions are independent of height (figure 18), contrary to the predictions of the stratification model.

4.2. *Structure factor*

The structure factors were calculated from particle positions within the viewing window using the 'Bounded' geometry, which allows for more accurate Fourier analysis in the horizontal plane. Figure 12 shows that, in comparison with the initial equilibrium distribution, horizontal density fluctuations are strongly suppressed by no-slip boundaries at the top and bottom of the container. A physical interpretation of the data in figure 12 is that, if the viewing window were divided into vertical slices of sufficient size, there would be exactly the same number of particles in each slice, rather than the expected variance of order of the number of particles in the slice. On the other hand, suspensions with periodic boundary conditions do not undergo significant changes in microstructure during settling (Ladd 1997). In particular, the structure factor remains finite at all wavelengths. The significance of these results is that they demonstrate that the macroscopic boundaries have a profound effect on the distribution of particles in the bulk suspension.

The structure factor in a settling suspension develops a strong anisotropy, as shown in figure 13. While the horizontal density fluctuations decay to zero at long wavelengths, roughly as $k_\perp^2$, the vertical fluctuations tend to a non-zero constant at small $k_\parallel$. Damping of horizontal density fluctuations at least as fast as $k_\perp^2$ is the minimum requirement for hydrodynamic screening, as was pointed out by Levine

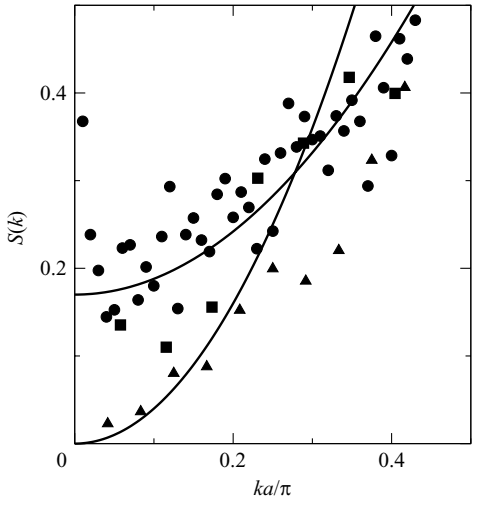

FIGURE 13. Structure factor at different angles; vertical [0,0,1] direction (circles), 45° [1,0,1] direction (squares), and horizontal [1,0,0] direction (triangles). The solid lines are quadratic fits to the vertical and horizontal fluctuations.

et al. (1998). They proposed that there are two qualitatively distinct non-equilibrium phases for settling suspensions, an unscreened phase characterized by a random microstructure and a screened phase where the long-wavelength density fluctuations in the horizontal plane are suppressed. They obtained an expression for the non-equilibrium structure-factor,

$$S(\boldsymbol{k}) = \frac{N_\perp k_\perp^2 + N_\parallel k_\parallel^2}{D_\perp k_\perp^2 + D_\parallel k_\parallel^2 + \gamma k_\perp^2 / k^2}, \tag{4.3}$$

which is consistent in functional form with the structure factor obtained in our numerical simulations (figure 13). The renormalized parameters – the fluctuations in particle flux N_i, the diffusion coefficients D_i, and the damping coefficient γ – were calculated from coupled field equations describing the evolution of the particle concentration and fluid velocity (Levine *et al.* 1998). According to the theory, the phase boundary is determined by the anisotropy in the renormalized noise, $N_\perp/N_\parallel$, and diffusivity, $D_\perp/D_\parallel$.

The structure factor data can be used to extract ratios of the parameters that appear in (4.3); namely, $N_\perp/\gamma = 0.4a^2$ and $N_\parallel/D_\parallel = 0.17$. We obtained $N_\perp/\gamma$ and $N_\parallel/D_\parallel$ from the low-k behaviour of the horizontal and vertical density fluctuations, but since our data are rather noisy, it is impossible to extract a meaningful value of $D_\perp/\gamma$, which appears as a quartic correction to the asymptotic k^2 dependence of the structure factor. Nevertheless, for the sake of completeness we will use our best estimate, $D_\perp/\gamma = 0.5a^2$, to determine the ratio $N_\perp/N_\parallel \approx 0.7$. When combined with tracer-diffusion measurements of $D_\perp/D_\parallel = 0.16$, this suggests we are near the transition between screened and unscreened phases (Levine *et al.* 1998). However, our data are not sufficiently precise to enable a definitive conclusion to be drawn. Significantly larger system sizes will be necessary for a quantitative comparison with the predictions of the theory, with greatly increased computational requirements.

Density fluctuations have also been calculated in other low-index directions; figure 13 also shows data for the 45° [1,0,1] direction. Unfortunately, the system is not

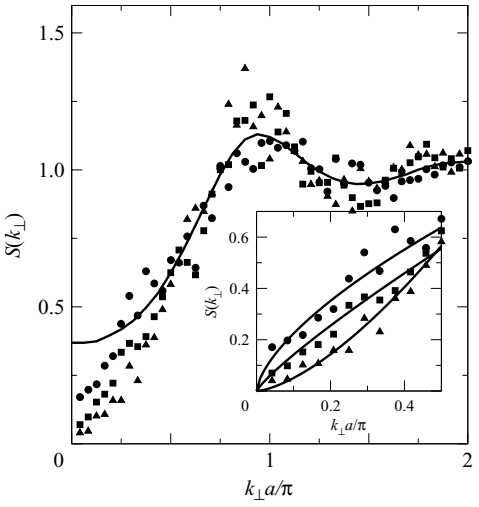

FIGURE 14. Time evolution of structure factor for horizontal density fluctuations. The structure factor was averaged over four different initial conditions and over successive intervals of $200t_s$; $0t_s$–$200t_s$ (circles), $200t_s$–$400t_s$ (squares), and $400t_s$–$600t_s$ (triangles). The solid line is the equilibrium distribution. The inset emphasizes the behaviour of $S(k_\perp)$ at long wavelengths.

periodic for any k-vector that lies outside the horizontal plane, so this data are inherently noisier than the [1,0,0] direction. Further complicating the analysis is the presence of a shoulder in $S(\boldsymbol{k})$, which is most clearly seen for the [1,0,0] direction at $ka \approx \pi/4$. For $ka > \pi/4$, the structure factor approaches the equilibrium distribution (see figure 12), but there is a sharp change to an asymptotic $k_\perp^2$ dependence when $ka < \pi/4$. This behaviour is consistent with the renormalized convection–diffusion model (Levine *et al.* 1998), with a transition between diffusive dynamics at shorter wavelengths and convective dynamics at long wavelengths. The data for the 45° direction may also be showing a shoulder at smaller k, $ka \approx \pi/6$, but a wider cell (smaller k-vectors) is necessary to confirm this. This is an important point, because hydrodynamic screening requires that the density fluctuations are damped in all directions except the vertical. In practice, this means the shoulder is expected to move to smaller and smaller k as the direction rotates from horizontal to vertical.

Although the structure factors measured in the simulations are consistent with the predictions of Levine *et al.* (1998), their theory postulates that all the important dynamics occurs in the bulk, independent of the macroscopic boundary conditions. Although this is a logical assumption, numerical simulations have shown that it is incorrect. Simulations with periodic boundary conditions (Ladd 1996, 1997) do not exhibit any damping of the horizontal density fluctuations, as would be expected if the model were correct in all essentials. Instead, our simulations suggest that the container bottom and the suspension–supernatant interface act as sinks of fluctuation energy, as suggested by Hinch (1988). Random density fluctuations convect to one of these two interfaces and are absorbed by the density gradient at the interface. The data shown in figure 14 support this conclusion, albeit not conclusively. Here we show the structure factor in the viewing window during its evolution from an equilibrium state to the steady state. Despite the limited time averaging (a total of $4 \times 200t_s = 800t_s$ for each plot), the implication is that the long wavelength fluctuations decay at a comparable rate to those at smaller scales. If so, this is evidence for the immediate convection

of large-scale density fluctuations (Hinch 1988), rather than the establishment of a density gradient by hydrodynamic diffusion (Mucha *et al.* 2004).

4.3. *Mean settling speed*

Our results suggest that the mean particle velocity decreases during settling by about 25%, as shown in figure 9. This happens whenever there is a no-slip wall bounding the top and bottom of the container, and is independent of system height (figure 6), Reynolds number (figure 9) and grid resolution (figure 10). To our knowledge, a systematic variation of settling velocity with time has not been reported previously, but it is consistent with a time-dependent reduction in number-density fluctuations, which has been observed experimentally (Lei *et al.* 2001). If the change in settling velocity is owing to changes in the microstructure at long wavelengths, then it can be estimated from the relation between the settling velocity and structure factor (Ladd 1993),

$$\langle \Delta U \rangle = \frac{6\pi U_0 a}{(2\pi)^3} \int [S(\boldsymbol{k}) - S_{eq}(k)] \left[\frac{k_x^2 + k_y^2}{k^4} \right] \mathrm{d}\boldsymbol{k}. \tag{4.4}$$

The steady-state structure factor was taken from (4.3) with the parameters determined from the simulation data (§4.2); the equilibrium structure factor was fitted by a quadratic polynomial. The integration was taken up to a maximum $ka = \pi/2$, beyond which it was assumed that the structure factors were similar. This model predicted a decrease in the mean settling speed of $\langle \Delta U \rangle = -0.20 U_0$ at $\phi = 0.13$, in reasonable agreement with the simulation result, $\langle \Delta U \rangle = -0.13 U_0$.

5. Polydisperse suspensions

The particles used in typical laboratory measurements have a polydispersity in the range 5–10% (Nicolai *et al.* 1995; Guazzelli 2001; Tee *et al.* 2002) although some experiments use significantly more monodisperse particles (Segré *et al.* 1997; Bernard-Michel *et al.* 2002). In a fluidized bed, it is well known that particles segregate according to size, with a denser suspension of larger particles at the bottom and a less dense suspension of smaller particles at the top. The larger particles have an inherently higher settling velocity and therefore match the fluidization velocity at a higher concentration than the smaller particles. Thus, a fluidized bed of polydisperse particles is inevitably stratified in both concentration and volume fraction. We have studied the settling of polydisperse suspensions to find out if there is significant segregation during the settling process, and what effects that may have on the velocity fluctuations and microstructure.

5.1. *Stratification*

Figure 15 shows the instantaneous density profiles in a 10% polydisperse suspension at steady state ($t = 1200 t_s$). In contrast to a monodisperse suspension (figure 11), the suspension–supernatant interface is considerably broader (figure 15*a*), and there is a weak underlying stratification of the particle volume fraction. The volume fraction profile is broken down in figure 15(*b*) into contributions from three different size ranges. It can be seen that there is considerable segregation by this time and the suspension–supernatant interface is dominated by the smallest particles. Small particles tend to drift into the upper region of the front, while the large particles settle faster and are absent from the front; medium-size particles are distributed throughout the suspension. We emphasize that the interface spreading seen in figure 15(*a*) is a result of differential convection of different particle sizes rather than hydrodynamic

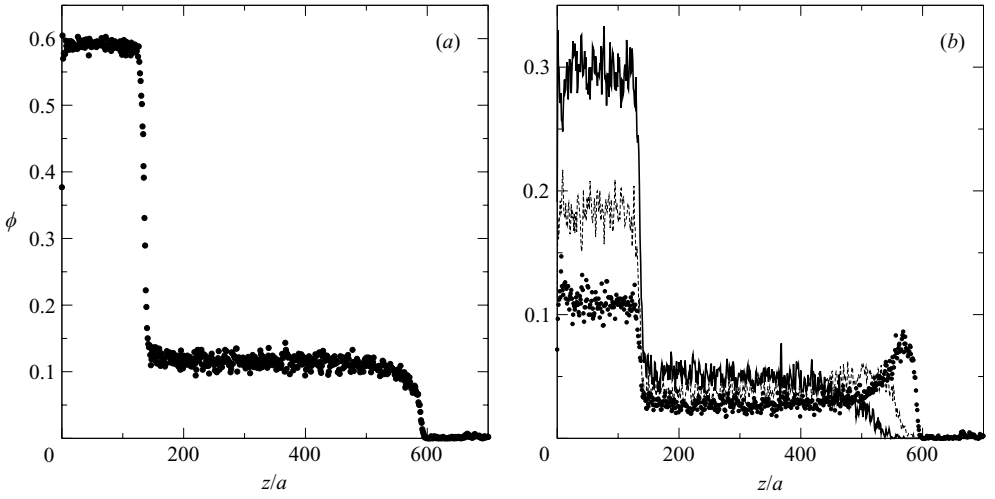

FIGURE 15. Profiles of the particle volume fractions as a function of the system height at $t = 1200t_s$. The overall volume fraction for a 10% polydisperse suspension is shown in (a). The volume fraction is shown separated into three size ranges in (b): large (solid line), medium (dotted line) and small (circles). Each range contains an equal number of particles.

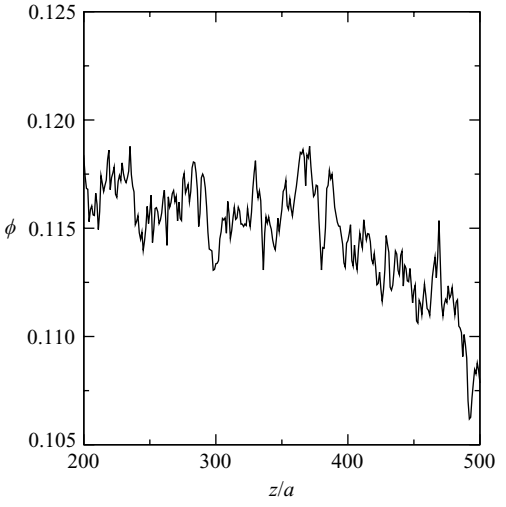

FIGURE 16. Particle volume fraction profile for a 10% polydisperse suspension at steady state, $1000 < t/t_s < 1400$. The density profile within typical viewing windows 200–500a is shown for the 'Box' geometry.

diffusion, which we have seen does not produce a broad interface at this volume fraction.

Our simulations show that there is a stratification of the particle mass density (or volume fraction) in polydisperse suspensions, which persists deep into the bulk as shown in figure 16. In comparison with the monodisperse suspension (figure 11), here there is a decrease of particle volume fraction with height, which is clearly visible over the statistical noise. The concentration profile can be modelled by a polydisperse convection–diffusion equation analogous to (4.2):

$$\partial_t \phi_i - \partial_z (U_i \phi_i) = \partial_z (D_\parallel \partial_z \phi_i), \tag{5.1}$$

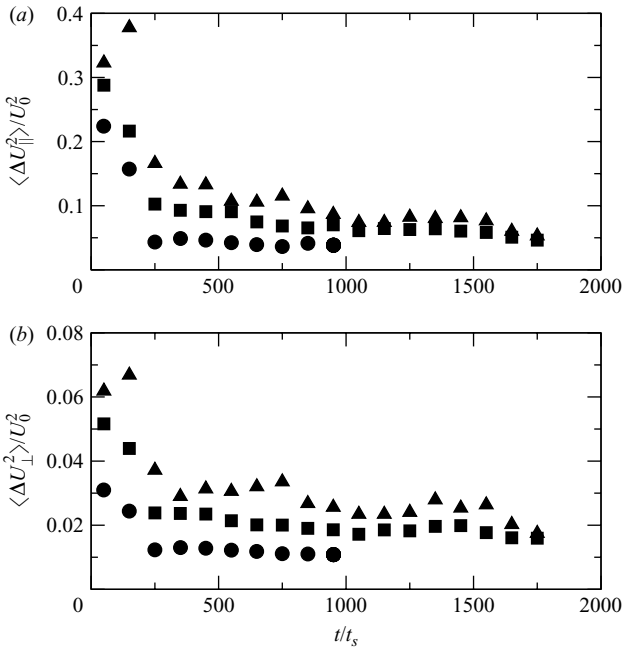

FIGURE 17. Particle velocity fluctuations as a function of time for a 10% polydisperse suspension. The data are taken within a window of height $250 \leqslant z/a \leqslant 400$ in the 'Box' geometry for three system widths: $W/a = 16$ (circles), 32 (squares) and 48 (triangles).

where the particle sizes have been divided into a number of different size ranges, with volume fraction ϕ_i and settling velocity $U_i = U_{i,0} f(\phi)$. The settling velocity was constructed from the usual approximation that takes the settling velocity of the isolated particle and a hindrance function, $f(\phi)$, based on the total volume fraction $\phi = \sum_i \phi_i$. In the absence of diffusion, $D_{\parallel} = 0$, we find an interface spreading and segregation that is qualitatively similar to the simulation data, confirming that polydispersity is the dominant mechanism for stratification at this volume fraction. Experimentally, convective spreading owing to polydispersity has been found to be more important than hydrodynamic diffusion (Bergougnoux *et al.* 2002), even at volume fractions less than 1%.

5.2. *Velocity fluctuations*

The concentration profile at the interface between a polydisperse suspension and the supernatant fluid is continually evolving during settling, so the designation of a steady state may be more arbitrary than in the monodisperse case. Nevertheless, there are time windows of about $400t_s$ duration when the velocity fluctuations are essentially stationary, as shown in figure 17. The velocity fluctuations are larger than in the monodisperse case (figure 8) as observed experimentally (Bernard-Michel *et al.* 2002), but the order of magnitude is the same. The anisotropy between vertical and horizontal velocity fluctuations is in the range 3–4 for polydisperse suspensions, comparable to experiment, while it is somewhat less for monodisperse suspensions. The velocity fluctuations in the different geometries are summarized in table 2.

The dependence of the velocity fluctuations on height are qualitatively different in monodisperse and polydisperse suspensions. Figure 18 shows that the velocity fluctuations in monodisperse suspensions are independent of vertical position in the bulk

	W/a	Box	Centre		Time (t_s)	Space (a)
$\langle \Delta U_{\parallel}^2 \rangle / \langle U_{\parallel} \rangle^2$	16	0.27	0.43	Box	600–1000	150–400
	32	0.49	0.65		800–1200	200–400
	48	0.60	0.95		1100–1500	250–400
$\langle \Delta U_{\perp}^2 \rangle / \langle U_{\parallel} \rangle^2$	16	0.08	0.12			
	32	0.14	0.24			
	48	0.19	0.34			

TABLE 2. Steady-state particle velocity fluctuations in a 10% polydisperse suspension as a function of system width. Fluctuations have been averaged over the whole cross-section in the column labelled 'Box' and along the centreline in the column labelled 'Centre' (cf. figure 7). The temporal and spatial windows used for averaging 'Box' geometry are shown in the last two columns.

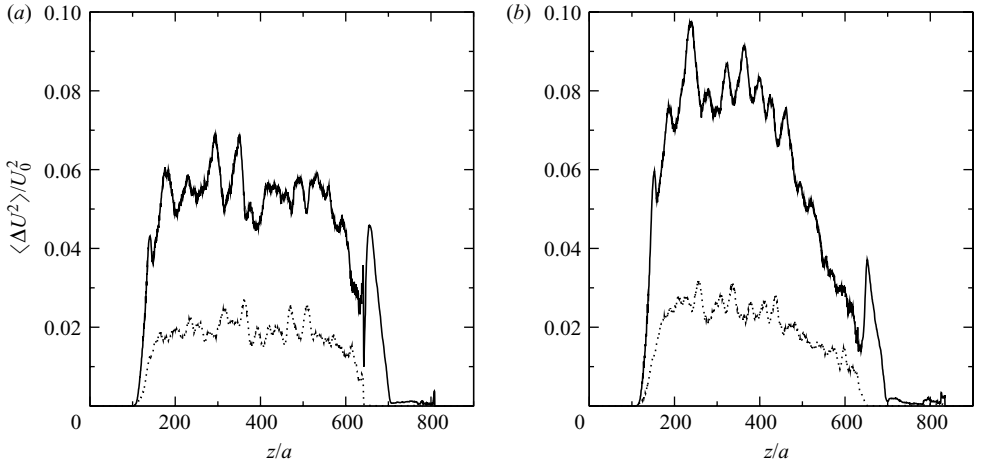

FIGURE 18. Comparison of particle velocity fluctuations for (a) monodisperse and (b) 10% polydisperse suspensions. The vertical (solid lines) and horizontal (dotted lines) velocity fluctuations are averaged over the horizontal plane for the duration of the steady state $1000 < t/t_s < 1400$. Results are shown as a function of height, z/a, for the 'Box' geometry, with $W = 48a$. ($N = 72\,000$).

suspension, while in polydisperse suspensions they decay with increasing height. Mucha *et al.* (2004) have pointed out that a stratified suspension is expected to lead to a reduction of the velocity fluctuations near the suspension–supernatant interface, because the density gradient is larger there (see figure 15a), and therefore more effective in damping the velocity fluctuations. The decreasing fluctuations shown in figure 18 are further evidence that the polydisperse suspension is stratified, while the monodisperse suspension is not.

The data in figures 16 and 18 indicate that the velocity fluctuations are controlled by stratification for $z > 400a$. The gradient in volume fraction, $\beta a = -\mathrm{d}(\log \phi)/\mathrm{d}z$, at $z = 400a$ is approximately 2.5×10^{-4}. According to the scaling arguments in Mucha *et al.* (2004), stratification controls the velocity fluctuations when β exceeds a critical stratification β_c, and at this point the velocity fluctuations should start to decay with height. The predicted critical stratification (Mucha *et al.* 2004),

$$\beta_c a = B(W/a)^{-5/2} \phi^{-1/2}, \tag{5.2}$$

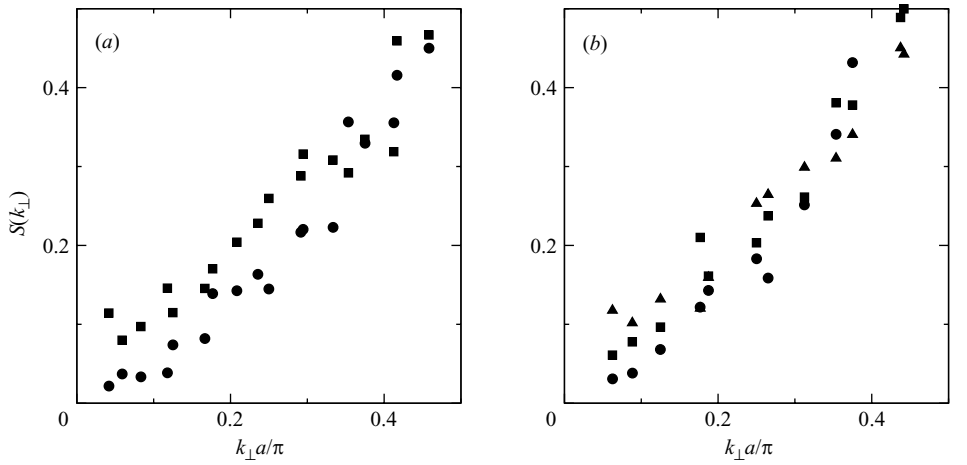

FIGURE 19. Comparison of structure factors for different degrees of polydispersity: (*a*) monodisperse (circles) and 10% polydisperse (squares) suspensions ($W = 48a$, $N = 72\,000$); (*b*) 2% (circles), 5% (squares) and 10% (triangles) polydisperse suspensions ($W = 32a$, $N = 32\,000$). Data were taken in the viewing window of 'Bounded' systems at steady state.

is $\beta_c \sim 2 \times 10^{-4} a^{-1}$ (taking the constant $B = 1$), which is consistent with the observed decay of the velocity fluctuations above this point.

The multi-species convection–diffusion equation (equation (5.1)) predicts a stratification $\beta a \sim 2 \times 10^{-4}$ for conditions corresponding to figure 16, in good agreement with the stratification observed in the simulation. The results from the convection–diffusion equation are insensitive to estimates of the diffusion coefficient in the range of numerical and experimental observations, $D/\langle U_\parallel \rangle a < 10$; in fact, similar stratification is observed without any hydrodynamic diffusion at all. These results demonstrate that polydisperse suspensions can stratify by size segregation, and that the stratification is sufficient to control the amplitude of the velocity fluctuations.

5.3. *Structure factor*

Our simulations show that small amounts of polydispersity destroy the delicate microstructural rearrangements observed in strictly monodisperse suspensions. Horizontal density fluctuations in significantly polydisperse suspensions are not damped at long wavelengths as they are for monodisperse suspensions, as shown in figure 19(*a*). This implies that there is more than one mechanism for hydrodynamic screening. In monodisperse suspensions, the distribution of particle pairs adjusts itself during settling so that the density fluctuations are damped as k^2 at long wavelengths. In polydisperse suspensions, the microstructure is apparently randomized by the varying settling speeds, but the particle velocity fluctuations are then damped by stratification (§ 5.2).

The structure factors for different degrees of polydispersity are compared in figure 19(*b*). The systems are smaller in this case and so there are fewer k-vectors. The structure factor for 2% polydispersity is similar to the monodisperse case, apparently vanishing as $k_\perp^2$ at long wavelengths. For higher degrees of polydispersity, 5% and 10%, the structure factor tends to a non-zero value at low $k_\perp$. It appears that only a small amount of polydispersity ($\sigma \sim 0.02$) can be tolerated if laboratory experiments are to mimic the properties of a monodisperse suspension.

Experiment	W/a	H/a	ϕ	σ	$\beta_D a$	$\beta_\sigma a$	$\beta_c a$
Nicolai 95	50	1250	0.05	0.043–0.065	1×10^{-4}	$0.1–2\times10^{-4}$	1×10^{-4}
	200				1×10^{-4}	$0.1–2\times10^{-4}$	4×10^{-6}
Segré 97	128	12 800	0.01	<0.02	6×10^{-6}	$<10^{-9}$	3×10^{-5}
			0.001		6×10^{-6}	$<10^{-9}$	9×10^{-5}
Guazzelli 01	1350	2700	0.0005	0.054–0.081	3×10^{-5}	$0.7–4\times10^{-4}$	3×10^{-7}
Tee 02	113	4830	0.01	0.067–0.100	2×10^{-5}	$1–3\times10^{-4}$	4×10^{-5}
	1330	45 300			5×10^{-7}	$1–3\times10^{-5}$	8×10^{-8}
Bernard-Michel 02	100	4000	0.01	<0.02	3×10^{-5}	$<10^{-9}$	5×10^{-5}
	100			0.070–0.105	3×10^{-5}	$1–4\times10^{-4}$	5×10^{-5}
	400			<0.02	3×10^{-5}	$<10^{-9}$	2×10^{-6}

TABLE 3. Estimates of stratification in laboratory experiments. Solutions of the convection–diffusion equation for a multi-component suspension (equation (5.1)) have been used to predict the stratification βa at a typical height for measurements $H/3$, and after a time when the suspension has settled to half its original height. For each system, we show the stratification produced by interface diffusion, β_D, and by segregation, β_σ, as well as the critical stratification, $\beta_c a$. The hydrodynamic diffusion coefficients were calculated from Eqs. 5.4 and 5.5, using the smallest container dimension as W.

5.4. *Stratification in laboratory experiments*

Solutions to (5.1) have also been used to estimate the degree of stratification in several sets of laboratory experiments. The calculations are by no means exhaustive nor are they quantitative; they describe only a range of possibilities based on a simple model for the time-dependent concentration profile. The goal is to understand in which experiments stratification may play a role, and whether it is predominately owing to interface diffusion or size segregation. The hindered settling function was calculated from the Richardson–Zaki expression,

$$f(\phi) = (1-\phi)^{5.5}, \tag{5.3}$$

but the hydrodynamic diffusion coefficient is more problematic. Measured hydrodynamic dispersion coefficients in settling suspensions are generally quite small, $D_\parallel < 10U_0 a$ (Davis & Hassen 1988; Nicolai *et al.* 1995). However, it has been pointed out (Mucha & Brenner 2003; Mucha *et al.* 2004) that the initial hydrodynamic diffusion coefficient may be much larger; the theory for a random suspension Koch (1994) gives

$$D_W = C\phi^{1/2}(W/a)^{3/2}U_0 a, \tag{5.4}$$

where C is a constant of order 1. However, a large diffusion coefficient promotes stratification, which will tend to reduce further hydrodynamic dispersion by suppressing the velocity fluctuations. We have therefore used the model proposed by Mucha & Brenner (2003) for the hydrodynamic diffusion, making $D_\parallel$ a function of the local stratification. When $\beta < \beta_c$ (equation (5.2)), $D_\parallel = D_W$, whereas for stratified regions, $\beta > \beta_c$,

$$D_\parallel = C\phi^{1/5}(B/\beta a)^{3/5}U_0 a. \tag{5.5}$$

We used the same proportionality constants as in Mucha & Brenner (2003); namely, $B = 0.5$ and $C = 1$.

Equations (5.1)–(5.5) were solved from an initially uniform spatial distribution; the size distribution was assumed to be Gaussian. The degree of polydispersity σ was taken in the range 1–1.5 times the reported standard deviation in particle size,

to account for additional variations in settling speed owing to variations in particle density and sphericity. The results in table 3 use a location one-third of the way up the vessel as the reference point, and a time when the front has fallen half the initial height.

Our calculations indicate that significant stratification can occur in most laboratory experiments, as shown in table 3. Size segregation introduces a convective mechanism for stratification, which is inherently more efficient over large distances than interface diffusion, and makes a comparable or larger contribution to stratification than interface diffusion in many cases. However, the degree of stratification is very sensitive to the level of polydispersity, which is difficult to quantify since there are additional contributions from variations in the density and shape of the particles. In general, critical stratification is exceeded when the effective polydispersity is larger than 4–5%. On the other hand, interface diffusion can cause significant stratification in suspensions where the aspect ratio of the cell, H/W, is less than 10.

6. Discussion and conclusions

The focus of this work has been to address the role of macroscopic boundary conditions on the microstructure of a settling suspension. We have found that, in monodisperse suspensions, there is a rearrangement of the pair distribution in the bulk region of the suspension, which suppresses the long-wavelength density fluctuations. Simulations with different macroscopic boundary conditions have demonstrated that walls at the top and bottom of the container play a crucial role in determining this distribution. The measured structure factor is consistent with the key qualitative features predicted theoretically by Levine *et al.* (1998) using a renormalized convection–diffusion model. However, this theory cannot yet explain why the macroscopic boundary conditions are a key component of the dynamics.

We have found no evidence for stratification in monodisperse suspensions at moderate concentrations. Our results suggest that the interface is sharp and that the concentration in the bulk is uniform. The suggestion (Mucha *et al.* 2004) that our earlier observations (Ladd 2002) could be explained in terms of stratification is incorrect, although we do not rule out the possible significance of interfacial diffusion in dilute suspensions ($\phi < 1\%$), such as are commonly used in particle-image-velocimetry measurements (Guazzelli 2001; Tee *et al.* 2002; Bernard-Michel *et al.* 2002). We conclude that there is a mechanism for microstructural rearrangement in the bulk of a monodisperse suspension, which leads to a substantial reduction in the amplitude of the velocity fluctuations from the predictions for randomly distributed particles. Our simulations are not large enough to show complete saturation, but the agreement with experimental measurements (Segré *et al.* 1997; Bernard-Michel *et al.* 2002) at comparable values of the cell size, $W/a\phi^{1/3}$, is good.

Most experiments use particles with significant polydispersity in size. In this case, our results show that the pair correlations are noticeably more random than in the monodisperse case and for $\sigma \geqslant 0.05$, the driving force for microstructural rearrangements is no longer sufficient to combat the additional randomization from variations in particle velocity. However, increasing polydispersity leads to significant stratification, even at moderate concentrations. Since, in this case, the stratification is driven by convective segregation of different particle sizes, it can spread over large distances, even in the presence of hindered settling. We suggest that segregation-induced stratification may have a profound effect on the interpretation of experimental measurements, even in dense suspensions.

Our simulations suggest that there is more than one screening mechanism at work in laboratory experiments, and that it is therefore crucial to control the conditions of the experiment, including the size and shape of the cell, the polydispersity of the particles, and the initial conditions. Large cells, dilute suspensions and highly monodisperse particles suggest stratification by interface diffusion will be important (Mucha & Brenner 2003; Mucha *et al.* 2004), while small amounts of polydispersity ($\sigma \geqslant 0.05$) will ensure stratification by size segregation in most instances. Moderate concentrations will suppress interface diffusion, because of hindered settling, but not stratification by size segregation. The shape of the sample cell may be important in setting the initial distribution of density fluctuations and thus cells with high width to depth ratios, may behave differently from square cells. There is limited experimental data where polydispersity is clearly negligible; only the experiments of Segré *et al.* (1997) and Bernard-Michel *et al.* (2002) use particles that are close to monodisperse. Moreover, Bernard-Michel *et al.* (2002) found that saturation was not clearly observed in very dilute suspensions. The fundamental question of the behaviour of the velocity fluctuations in monodisperse suspensions therefore remains unsettled.

We would like to thank Élisabèth Guazzelli, John Hinch and Peter Mucha for helpful discussions in the preparation of this manuscript. The work was supported by the Microgravity Biological and Fluids Physics Division of the National Aeronautics and Space Administration.

REFERENCES

Aidun, C. K., Lu, Y. N. & Ding, E. 1998 Direct analysis of particulate suspensions with inertia using the discrete Boltzmann equation. *J. Fluid Mech.* **373**, 287–311.

Bergougnoux, L., Ghicini, S., Guazzelli, E. & Hinch, J. 2002 Spreading fronts and fluctuations in sedimentation. *Phys. Fluids* **15**, 1875–1887.

Bernard-Michel, G., Monavon, A., Lhuillier, D., Abdo, D. & Simon, H. 2002 Particle velocity fluctuations and correlation lengths in dilute sedimenting suspensions. *Phys. Fluids* **14**, 2339–2349.

Bouzidi, M., Firdaouss, M. & Lallemand, P. 2001 Momentum transfer of a Boltzmann-lattice fluid with boundaries. *Phys. Fluids* **13**, 3452–3459.

Brady, J. F. & Bossis, G. 1988 Stokesian dynamics. *Annu. Rev. Fluid. Mech.* **20**, 111.

Brenner, M. P. 1999 Screening mechanisms in sedimentation. *Phys. Fluids* **11**, 754–772.

Caflisch, R. E. & Luke, J. H. C. 1985 Variance in the sedimentation speed of a suspension. *Phys. Fluids* **28**, 759.

Cowan, M. L., Page, J. H. & Weitz, D. A. 2000 Velocity fluctuations in fluidized suspensions probed by ultrasonic correlation spectroscopy. *Phys. Rev. Lett.* p. 453456.

Davis, R. H. & Hassen, M. A. 1988 Spreading of the interface at the top of a slightly polydisperse sedimenting suspension. *J. Fluid Mech.* **196**, 107.

Durlofsky, L., Brady, J. F. & Bossis, G. 1987 Dynamic simulation of hydrodynamically interacting particles. *J. Fluid Mech.* **180**, 21.

Feng, J., Hu, H. H. & Joseph, D. D. 1994*a* Direct simulation of initial-value problems for the motion of solid bodies in a Newtonian fluid. 1. Sedimentation. *J. Fluid Mech.* **261**, 95–134.

Feng, J., Hu, H. H. & Joseph, D. D. 1994*b* Direct simulation of initial-value problems for the motion of solid bodies in a Newtonian fluid. Part 2. Couette and Poiseuille flows. *J. Fluid Mech.* **277**, 271–301.

Frisch, U., d'Humières, D., Hasslacher, B., Lallemand, P., Pomeau, Y. & Rivet, J.-P. 1987 Lattice gas hydrodynamics in two and three dimensions. *Complex Systems* **1**, 649.

Ginzbourg, I. & d'Humières, D. 2003 Multireflection boundary conditions for lattice Boltzmann models. *Phys. Rev.* E **68**, 066614.

Guazzelli, E. 2001 Evolution of particle-velocity correlations in sedimentation. *Phys. Fluids* **13**, 1537–1540.

Ham, J. M. & Homsy, G. M. 1988 Hindered settling and hydrodynamic dispersion in quiescent sedimenting suspensions. *Intl J. Multiphase Flow* **14**, 533.

Higuera, F., Succi, S. & Benzi, R. 1989 Lattice gas dynamics with enhanced collisions. *Europhys. Lett*. **9**, 345.

Hinch, E. J. 1988 Sedimentation of small particles. In *Disorder and Mixing* (ed. E. Guyon, Y. Pomeau & J. P. Nadal), pp. 153–161. Kluwer.

Hoogerbrugge, P. J. & Koelman, J. M. V. A. 1992 Simulating microscopic hydrodynamic phenomena with dissipative particle dynamics. *Europhys. Lett*. **19**, 155.

Jayaweera, K. O. L. F., Mason, B. J. & Slack, G. W. 1964 Behaviour of clusters of spheres falling in a viscous fluid. *J. Fluid Mech.* **20**, 121.

Kim, I., Elghobashi, S. & Sirignano, W. A. 1993 Three-dimensional flow over two spheres placed side by side. *J. Fluid Mech.* **246**, 465.

Koch, D. L. 1994 Hydrodynamic diffusion in a suspension of sedimenting point particles with periodic boundary conditions. *Phys. Fluids* A **6**, 2894.

Koch, D. L. & Shaqfeh, E. S. G. 1991 Screening in sedimenting suspensions. *J. Fluid Mech.* **224**, 275.

Ladd, A. J. C. 1993 Dynamical simulations of sedimenting spheres. *Phys. Fluids* A **5**, 299.

Ladd, A. J. C. 1994*a* Numerical simulations of particulate suspensions via a discretized Boltzmann equation. Part 1. Theoretical foundation. *J. Fluid Mech.* **271**, 285.

Ladd, A. J. C. 1994*b* Numerical simulations of particulate suspensions via a discretized Boltzmann equation. Part 2. Numerical results. *J. Fluid Mech.* **271**, 311.

Ladd, A. J. C. 1996 Hydrodynamic screening in sedimenting suspensions of non-Brownian spheres. *Phys. Rev. Lett*. **76**, 1392.

Ladd, A. J. C. 1997 Sedimentation of homogeneous suspensions of non-Brownian spheres. *Phys. Fluids* **9**, 491–499.

Ladd, A. J. C. 2002 Effects of container walls on the velocity fluctuations of sedimenting spheres. *Phys. Rev. Lett*. **88**, 048301.

Ladd, A. J. C. & Verberg, R. 2001 Lattice-Boltzmann simulations of particle–fluid suspensions. *J. Stat. Phys.* **104**, 1191–1251.

Lei, X., Ackerson, B. J. & Tong, P. 2001 Settling statistics of hard sphere particles. *Phys. Rev. Lett*. **86**, 3300–3303.

Levine, A., Ramaswamy, S., Frey, E. & Bruinsma, R. 1998 Screened and unscreened phases in sedimenting suspensions. *Phys. Rev. Lett*. **81**, 5944.

Loewenberg, M. & Hinch, E. J. 1996 Numerical simulation of a concentrated emulsion in shear flow. *J. Fluid Mech.* **321**, 395–419.

Lowe, C. P., Frenkel, D. & Masters, A. J. 1995 Long-time tails in angular momentum correlations. *J. Chem. Phys.* **103**, 1582–1587.

Luke, J. H. C. 2000 Decay of velocity fluctuations in a stably stratified suspension. *Phys. Fluids* **12**, 1619–1621.

Mucha, P. J. & Brenner, M. P. 2003 Diffusivities and front propagation in sedimentation. *Phys. Fluids* **15**, 1305.

Mucha, P. J., Tee, S.-Y., Weitz, D. A., Shraiman, B. I. & Brenner, M. P. 2004 A model for velocity fluctuations in sedimentation. *J. Fluid Mech.* **501**, 71–104.

Muldowney, G. P. & Higdon, J. J. L. 1995 A spectral boundary-element approach to 3-dimensional Stokes flow. *J. Fluid Mech.* **298**, 167–192.

Nguyen, N.-Q. & Ladd, A. J. C. 2002 Lubrication corrections for in lattice-Boltzmann simulations of particle suspensions. *Phys. Rev.* E **66**, 046708.

Nguyen, N.-Q. & Ladd, A. J. C. 2004 Microstructure in a settling suspension of hard spheres. *Phys. Rev.* E **69**, 050401(R).

Nicolai, H. & Guazzelli, E. 1995 Effect of the vessel size on the hydrodynamic diffusion of sedimenting spheres. *Phys. Fluids* **7**, 3.

Nicolai, H., Herzhaft, B., Hinch, E. J., Oger, L. & Guazzelli, E. 1995 Particle velocity fluctuations and hydrodynamic self-diffusion of sedimenting non-Brownian spheres. *Phys. Fluids* **7**, 12.

Pozrikidis, C. 1993 On the transient motion of ordered suspensions of liquid drops. *J. Fluid Mech.* **246**, 301–320.

Ramaswamy, S. 2001 Issues in the statistical mechanics of steady sedimentation. *Adv. Phys.* **50**, 297–341.

Rohde, M., Kandhai, D., Jerksen, J. J. & van den Akker, H. E. A. 2003 Improved bounce-back methods for no-slip walls in the lattice Boltzmann schemes: theory and simulations. *Phys. Rev.* E **67**, 066703.

Segré, P. N., Herbolzheimer, E. & Chaikin, P. M. 1997 Long-range correlations in sedimentation. *Phys. Rev. Lett.* **79**, 2574.

Tee, S. Y., Mucha, P. J., Cipelletti, L., Manley, S., Brenner, M. P., Segré, P. N. & Weitz, D. A. 2002 Nonuniversal velocity fluctuations of sedimenting particles. *Phys. Rev. Lett.* **89**, 054501–1.

Tong, P. & Ackerson, B. J. 1998 Analogies between colloidal sedimentation and turbulent convection at high Prandtl numbers. *Phys. Rev.* E **58**, R6931–R6934.

Verberg, R. & Ladd, A. J. C. 2001 Accuracy and stability of a lattice-Boltzmann model with sub-grid scale boundary conditions. *Phys. Rev.* E **65**, 016701.

Wu, J. & Manasseh, R. 1998 Dynamics of dual-particles settling under gravity. *Intl J. Multiphase Flow* **24**, 1343–1358.

Zhu, Y., Fox, P. J. & Morris, J. P. 1999 A pore-scale numerical model for flow through porous media. *Intl J. Numer. Anal. Methods Geomech.* **23**, 881–904.